Applied Energy 373 (2024) 123913

Contents lists available at ScienceDirect

Applied Energy

journal homepage: www.elsevier.com/locate/apenergy

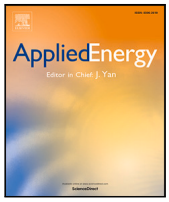

Multiscale multiphysics modeling of ammonia-fueled solid oxide fuel cell: Effects of temperature and pre-cracking on reliability and performance of stack and system

Arash Nemati [a,*], Omid Babaie Rizvandi [a,b], Rafael Nogueira Nakashima [a], Javid Beyrami [a], Henrik Lund Frandsen [a]

[a] Department of Energy Conversion and Storage, Technical University of Denmark, Fysikvej, DK-2800 Kgs. Lyngby, Denmark
[b] Mechanical Engineering Department, Colorado Fuel Cell Center, Colorado School of Mines, Golden, CO 80401, USA

ARTICLE INFO

Keywords:
Solid oxide fuel cell stack
Ammonia fuel
Operating temperature
Ammonia pre-cracking
Nitriding
System modeling

ABSTRACT

Ammonia is a promising carbon-free fuel for solid oxide fuel cells (SOFCs). However, direct feeding of ammonia into the SOFC may lead to serious degradation due to the nitriding. Conversely, the pre-cracking of ammonia introduces complexity to the system design and causes increased power losses in the system. Therefore, it is crucial to explore all these aspects simultaneously. In this context, this study introduces a novel multiscale modeling approach by integrating a 3D multiphysics simulation of the ammonia-fueled SOFC stack with system-level modeling to investigate the reliability and performance of the stack and system. Two different cell technologies developed for low temperature (LT) and high temperature (HT) operation are investigated at LT (600 – 700 °C) and HT (700 – 800 °C) ranges. The results indicate that fuel inlet temperature should be 55 °C and 18 °C higher than the minimum temperature in 0% pre-cracking case for HT and LT cases, respectively. The increase in the required air flow rate for cooling in the 100% pre-cracking case compared to the 0% pre-cracking case is around 100% and 216% for the HT and LT cases, respectively. However, stack power production and power losses in the system components are comparable for LT and HT cases which leads to similar system performance. A larger share of the active area is affected by nitriding in LT cases than HT ones. However, a smaller cracking ratio at LT (~ 82%) compared to HT conditions (~ 92%) is needed for elimination of nitriding. While the LT and HT cases are comparable in terms of system power production, the lower stack outlet temperatures in LT cases require novel and more expensive catalysts for ammonia pre-cracking and HT cases need more expensive steels.

1. Introduction

It is crucial to develop sustainable and environmentally friendly solutions to meet the world's energy demand while minimizing the negative impacts [1]. Fuel cells, as an appealing power-generation technology, are renowned for their clean, environmentally friendly characteristics, and high conversion efficiency [2]. Among the various fuel cell technologies, solid oxide fuel cells (SOFCs) have shown improved reaction kinetics and higher efficiencies, making them a promising candidate for various applications, including power generation and auxiliary power units [3]. Their high operating temperature enables efficient electrochemical reactions and facilitates the utilization of a wide range of fuels such as hydrogen, methane, methanol, ammonia, etc. [4].

Ammonia (NH_3) emerges as a promising carbon-free fuel for SOFCs, offering several advantageous properties such as easier liquefaction, lower flammability, and simpler transportation compared to hydrogen [5]. As a hydrogen carrier, ammonia consists of 17.6% hydrogen by weight [6]. It can be transported and stored in liquid form at 20 °C under 8.6 bars [7], and at −33 °C under 1 bar pressure [8]. It was also shown that NO_x emissions were not formed under SOFC conditions [9] which is one of the main challenges in ammonia-fueled internal combustion engines. However, one of the drawbacks of ammonia is its highly toxic nature, which makes it difficult and more expensive to handle [10].

In SOFCs, ammonia fuel commonly undergoes two distinct pathways, outlined as follows: 1- The endothermic cracking of NH_3 into N_2 and H_2 takes place within the nickel (Ni) based anode layers inside the SOFC. This pathway is usually referred to as direct ammonia-fueled SOFCs. 2- Ammonia is initially cracked into N_2 and H_2 in an external cracker. This method is referred to as the pre-cracked ammonia-fueled SOFC in this study.

* Corresponding author.
E-mail address: arnem@dtu.dk (A. Nemati).

https://doi.org/10.1016/j.apenergy.2024.123913
Received 21 February 2024; Received in revised form 11 June 2024; Accepted 11 July 2024
Available online 23 July 2024

Nomenclature

Abbreviation

3D	3 dimensional
AOR	Anode off-gas recirculation
ASR	Area specific resistance
BV	Butler–Volmer
DOF	Degrees of freedom
EIS	Electrochemical impedance spectroscopy
FCC	Face Centered Cubic
HCP	Hexagonal Close Packed
HT	High temperature
LT	Low temperature
OCV	Open circuit voltage
slpm	Standard liter per minute
SOFC	Solid oxide fuel cell

Symbols

$\dot{n}$	Molar flow rate
$\dot{W}$	Power
$\mathbf{u}$	Velocity vector
c	Heat capacity
D	Diffusion coefficient
E	Activation energy
F	Faraday's constant
G	Gibbs free energy
H	Enthalpy
h	Specific enthalpy
J	Current density
K_n	Nitriding potential
K	Nitriding potential
k	Thermal conductivity
M	Molar mass
P	Power
P	Pressure
Q	Heat
R	Gas constant
R	Reaction rate
S	Contact area density
S	Source term
T	Temperature
V	Voltage
w	Mass fraction
x	Mole fraction

Greek letters

Δ	Variation
η	Overpotential
μ	Dynamic viscosity
∇	Vector differential operator
ρ	Density
σ	Electric conductivity

Subscripts and superscripts

act	Activation
an	Anode
cat	Cathode
$conc$	Concentration
cr	Critical
eff	Effective
H_2	Hydrogen
H_2O	Water steam
NH_3	Ammonia
O_2	Oxygen
ohm	Ohmic
ref	Reference

Each of these pathways comes with its own set of advantages and disadvantages. In direct ammonia-fueled SOFCs, the need for installing an external cracker, which can be expensive and complex, is eliminated. Additionally, the endothermic cracking of ammonia contributes to the cooling of the SOFC stack, resulting in reduced air flow rates needed for stack cooling and consequently lower power losses in the air supply unit. On the other hand, high temperature gradients due to the endothermic cracking of ammonia leads to an increase in the tensile stresses in the SOFC stack [11]. Ni nitriding in the anode layers is also one of the main challenges in the direct feeding of ammonia to the SOFC stack, which leads to the degradation of the SOFC performance [12] and will mechanically degrade the Ni contacting layers on the fuel side. Pre-cracked ammonia-fueled SOFCs do not encounter the nitriding issue in the SOFC stack. However, they do require an external cracker and higher air flow rates to cool down the SOFC stack.

Ni nitriding can be highly problematic for the Ni-based contact layers and anodes in NH_3-fueled SOFCs. The Ni nitrides have a larger unit cell as compared to Ni itself, leading to local expansion in the material, which plastically deforms the ambient Ni. Ni nitrides can be unstable, and when decomposing, the shrinkage leaves pits on the deformed Ni surfaces. Repetitive nitriding-decomposition cycles of Ni can result in substantial microstructural changes of the Ni [12]. The irreversible degradation caused by these microstructural changes can lead to a decrease in the robustness of the contact layers and cells, as well as cell performance [13].

Some studies illustrated the possibility of nitriding occurring in other components of the SOFC stack, such as metal parts and interconnects. A 1000 h stability test was conducted on a direct ammonia-fueled SOFC stack consisting of 30 planar anode-supported cells at 750 °C [14]. The analysis revealed that the metallic interconnect was nitrided on the anode side i.e. a significant deformation and Fe-rich particles were observed on the surface.

The performance of a SOFC can be significantly influenced by its operating conditions. Various studies have been conducted in the literature focusing on ammonia-fueled SOFCs. Stoeckl et al. [15] conducted a performance evaluation of ammonia as a fuel for SOFCs with Ni-YSZ anodes. They compared the performance of the direct ammonia operation with the equivalent pre-cracked ammonia at 700, 750, and 800 °C. They concluded that, based on electrochemical impedance spectroscopy (EIS) analysis, the performance reduction of the direct ammonia-fueled cases compared to pre-cracked cases was a result of the endothermic ammonia cracking. They also observed nickel nitriding in the anode micro-structure, which was lower at 800 °C than 700 °C. They suggested that beside the faster cracking of ammonia inside the cells, this could be also a result of the higher thermal cracking of the ammonia stream before reaching the anode at higher temperatures [15].

In another study, Stoeckl et al. [16] investigated the performance and durability of an ammonia-fueled MK352 SOFC stack [17] with electrolyte-supported cells and chromium-based interconnects. They maintained the air outlet temperature at 835 °C and observed 18.8 °C temperature reduction at the inlet region of the stack due to the endothermic cracking of ammonia. They observed nitriding effects on

the nickel contact meshes and chromium nitrides were found in the material structure of the interconnects.

A SOFC operating at low temperatures (≤650 °C) enables the utilization of inexpensive interconnects and sealing materials [18]. It also facilitates rapid thermal cycling, reduces thermal stresses, enhances reliability and safety, and broadens its potential applications to include transportation and portable devices [19,20]. Reducing the operational temperature has the potential to boost the theoretical energy efficiency of a SOFC [21]. There are a lot of studies on the material development for low temperature SOFCs and some major SOFC developers like Ceres Power and Elcogen provide this kind of low temperature cell technology.

Numerical models play a crucial role as a complementary tool in gaining deeper insights into the complex phenomena that occur in SOFCs. Kishimoto et al. [22] conducted a comparison between direct and pre-cracked ammonia-fueled SOFCs in a 2D cell model and concluded that the slight decrease in the performance of the direct ammonia-fueled SOFC compared to its pre-cracked counterpart could be attributed to the temperature reduction (around 20 °C) originating from the endothermic cracking of ammonia [22]. Oh et al. [23] performed a comprehensive investigation of direct ammonia-fueled thin-film SOFCs using a 2D Multiphysics model. The authors concluded that a limited supply of hydrogen caused by reduced ammonia cracking at lower temperatures (≤650 °C), coupled with inadequate mass transport, led to a significant decline in the performance of direct ammonia-fueled thin-film SOFC.

In the final application, the ammonia-fueled SOFC is expected to be integrated into a system comprising air and fuel supply units, heat exchangers, and an external cracker for the pre-cracked ammonia-fueled SOFC.

Several studies have been conducted on the system-level modeling of ammonia-fueled SOFCs [24–27]. In the analysis of ammonia-fueled SOFC systems, 0D models are commonly employed in the existing literature. Even in the available 1D and 2D models, only the active area of the SOFC is usually taken into account. All these modeling and assumptions result in deviations from reality. For example, while considering a range for operating temperature (for instance 700–800 °C), usually the inlet temperature of SOFC is considered to be equal to the minimum of the range (700 °C) and a linear variation is considered from the inlet to outlet [27–29]. Furthermore, the outlet temperature of the SOFC is usually considered as the maximum temperature (i.e. 800 °C) which may not be correct and leads to variation in the thermal balance of the system. In reality, the temperature distribution is not linear, and inlet, outlet, and distribution of temperature are highly dependent on the operating conditions in the direct ammonia-fueled SOFCs. In addition, 3D multiphysics modeling can be used as a complementary and reliable tool to predict thermal stresses and simulation of possible fractions in the cells and sealing which is out of the scope of this study and will be addressed in the future. The pressure drops in the SOFC stack also can be calculated more accurately in the 3D multiphysics simulation which is not the case in other simplified models.

Based on the reviewed literature, no investigations have examined how different operating temperatures and cell technologies impact system performance and the selection of system components. Furthermore, the coupling of detailed 3D modeling of SOFC stack and system-level modeling to achieve a more realistic and comprehensive understanding of different aspects of ammonia-fueled SOFC systems is not available in the literature.

In this context, the current study introduces a novel multiscale approach that combines 3D multiphysics simulation of SOFC cells and stack with system-level modeling. The model developed in this study is employed to explore the impact of operating temperature and ammonia pre-cracking ratio on the performances of both the SOFC stack and the overall system and investigate different aspects such as nitriding issues. Two different cell technologies designed for low and high temperature operation are investigated to determine whether the low-temperature SOFC technology can improve the system's performance. The paper is organized as follows. The subsequent section describes the numerical modeling approach and the implemented models. In the results section, the model is initially employed to examine the impact of SOFC operating temperature and inlet fuel composition on the performance of the SOFC stack. Different parameters in the SOFC stack such as species, current density, and resistances are studied under various operating temperatures. Subsequently, nitriding as one of the main challenges in ammonia-fueled SOFCs is addressed. Finally, the results of the system-level modeling are presented.

2. Numerical modeling

This section provides a description of the numerical models and approaches used in the current study. This section is organized as follows:

- Section 2.1: describes the ammonia cracking rate model.
- Section 2.2: explains the nitriding degradation evaluation for both Ni and iron (in the steel components).
- Section 2.3: describes the cell level electro-chemical model.
- Section 2.4: presents the stack level model.
- Section 2.5: presents the system level model.
- Section 2.6: describes the coupling between different levels of modeling.

Eventually, all levels of simulation are embedded into a multi-scale model, making it possible to assess system performance and at the same time the nitriding at various locations inside the cells at different locations in the stacks for a given operating condition.

A schematic of the concept of the developed multiscale multiphysics modeling of ammonia-fueled SOFC is presented in Fig. 1. Different levels of the developed model including cell level, stack level, and system level are shown in this figure. The details of the different levels will be explained in the sections below.

2.1. Ammonia cracking rate

Ammonia cracking rate plays an important role in the performance of the ammonia-fueled SOFCs, as it directly impacts the distributions of hydrogen and temperature across the active area of the SOFC. At high temperatures (600–900 °C), which generally fall within the operating range of SOFCs, ammonia can undergo endothermic cracking. Thus, the cracking should be evaluated at every point inside all of the fuel electrodes in the SOFC stacks. This is effectively handled by the approach described in Ref. [11]. For a specific location inside the Ni-YSZ layers of the cells (see Fig. 1), ammonia cracking is described by the following expression [30]:

$$R_{crack}^{\mathrm{Ni-YSZ}} = 98.4 S_{\mathrm{Ni}-pore} exp\left(-\frac{E}{RT}\right) P_{\mathrm{NH_3}}^{0.69} (P_{\mathrm{H_2}} + 750)^{-0.39} \quad (1)$$

where, $R_{crack}^{\mathrm{Ni-YSZ}}$ is the ammonia cracking rate in Ni-YSZ layers in [mol/m^3 s], $S_{\mathrm{Ni}-pore}$ is the Ni-pore contact area density in [μm^2/μm^3], E is the activation energy equal to 1.2×10^5 in [kJ/mol], $P_{\mathrm{NH_3}}$ and $P_{\mathrm{H_2}}$ are the partial pressures of ammonia and hydrogen in [Pa], respectively. For $S_{\mathrm{Ni}-pore}$ the value of 0.88 measured by Trini et al. [31] is used in the current model.

The heat sink (Q) resulting from endothermal cracking in the regions, where ammonia cracking occurs is estimated by [32]:

$$Q = R_{crack}^{\mathrm{Ni-YSZ}} \Delta H \quad (2)$$

where ΔH is the enthalpy change associated with the ammonia cracking reaction. Validation of ammonia cracking rate on Ni-YSZ layers is presented in Appendix A.

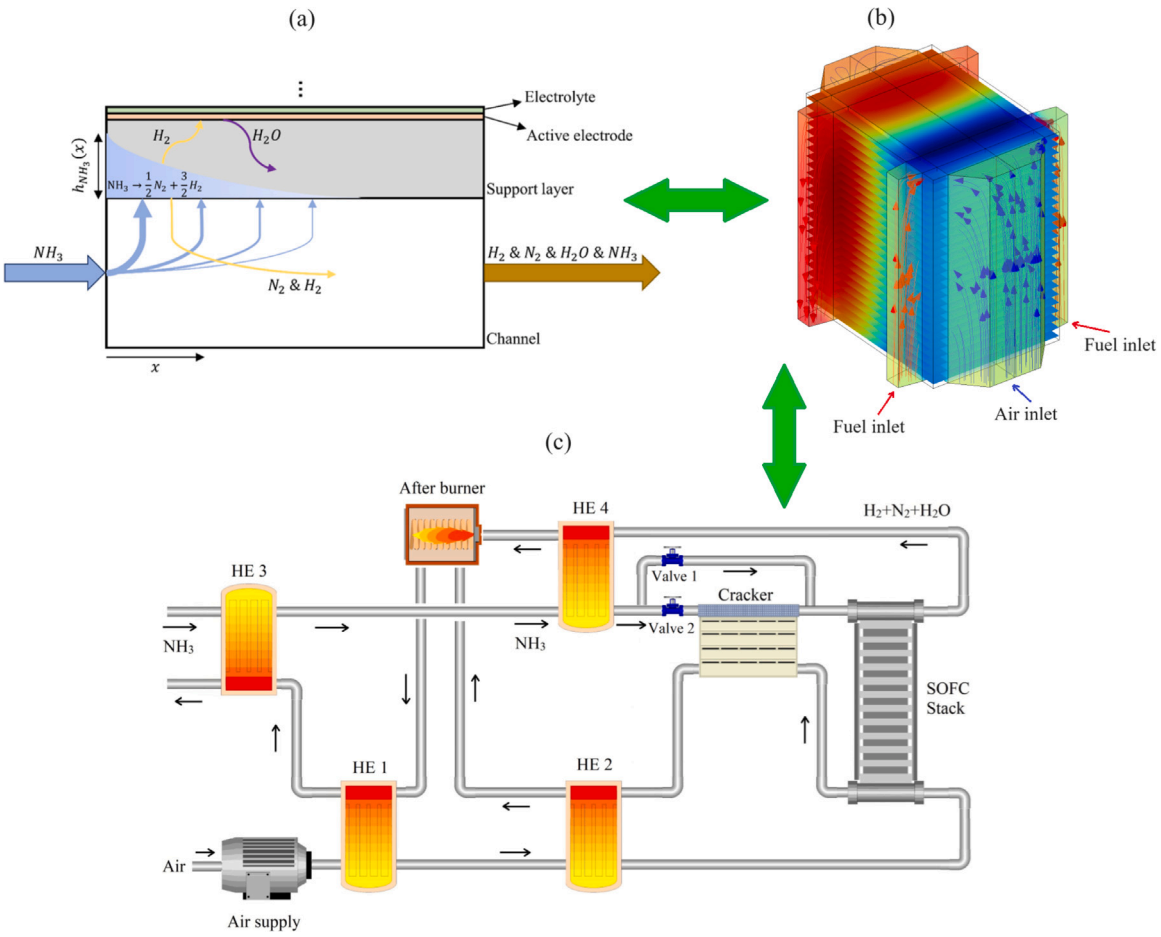

Fig. 1. Schematic of the concept of the multiscale multiphysics modeling of ammonia-fueled SOFC: (a) cell level [11], (b) stack level, and (c) system level.

2.2. Nitriding potential

Nitriding may have a harmful effect on Ni-containing layers [12] and metal parts [14] in the direct ammonia-fueled SOFCs. Therefore, a better understanding of the nitriding process helps us to protect the cells and metal interconnects under direct ammonia-fed operating conditions.

The Lehrer diagram [33] is a tool used to describe the phase stabilities in pure iron based on temperature. It provides valuable information about the formation of different nitride phases in iron and can be customized to determine the process control parameters for gas nitriding in steels [34,35].

Based on the customized Lehrer diagram for Ni [36] obtained from Thermo-Calc software, there are two stable phases that exist in the Ni-rich part of the Ni-N system. The Face Centered Cubic (FCC), and the Ni_3N phase, which is Hexagonal Close Packed (HCP) [37,38]. Nitrogen can dissolve in pure Ni forming the FCC solid solution first, and then the HCP phase begins to form with an increase of nitrogen concentration in the binary system as a consequence. The stability of the FCC solid solution is determined by temperature and nitrogen concentration.

The nitriding potential (K_n), which is a parameter that specifies where nitriding will occur, is defined as follows:

$$K_n = \frac{x_{\mathrm{NH_3}}}{x_{\mathrm{H_2}}^{1.5}} \tag{3}$$

where, $x_{\mathrm{NH_3}}$ and $x_{\mathrm{H_2}}$ are the mole fractions of ammonia and hydrogen, respectively. The variation of $K_{n,critical}$ ($K_{n,cr}$) which is the interface between these two phases is presented in Fig. 2a. The stability of the FCC phase ($K_{n,cr}$) decreases with temperature, which means that the FCC phase is more readily transformed to the HCP phase at higher temperatures.

To avoid Ni nitriding, the HCP phase should be avoided. Therefore, the safe region is the region, where K_n (Eq. (3)) is lower than $K_{n,cr}$:

$$K_n < K_{n,cr} \Rightarrow \frac{K_n}{K_{n,cr}} < 1 \tag{4}$$

The critical nitriding potential ($K_{n,cr}$) for Fe [39] as one of the main components of metal parts is also presented and compared with $K_{n,cr}$ of Ni in Fig. 2b. Here it is assumed that the nitriding of the metals in the stack can be modeled as the nitriding of the iron, in lack of more precise investigations. Often the interconnects are not coated on the fuel side, so the assumption is deemed reasonable. As can be seen, the $K_{n,cr}$ for Fe is lower than that for Ni, which suggests a higher chance of nitriding on Fe than Ni surfaces.

2.3. Cell level modeling for finding the properties of cell

Two kinds of cell technologies are investigated in the current numerical study. One of the cells is a cell developed at DTU for high temperature and another one is a cell developed for lower temperature conditions developed at Elcogen. The main difference between the low temperature and high temperature cells is the thickness of the electrolyte. The electrolyte thickness for low temperature cells is 3–6 μm [40], while this thickness is around 10 μm [41] for the high temperature cells. Thinner electrolyte for low temperature cells leads to lower resistance than high temperature cells under the same conditions. Another difference is the material of the air electrode. In the low temperature cells, Lanthanum Strontium Cobaltite (LSC) [40] is used in the air electrode instead of Lanthanum strontium cobalt

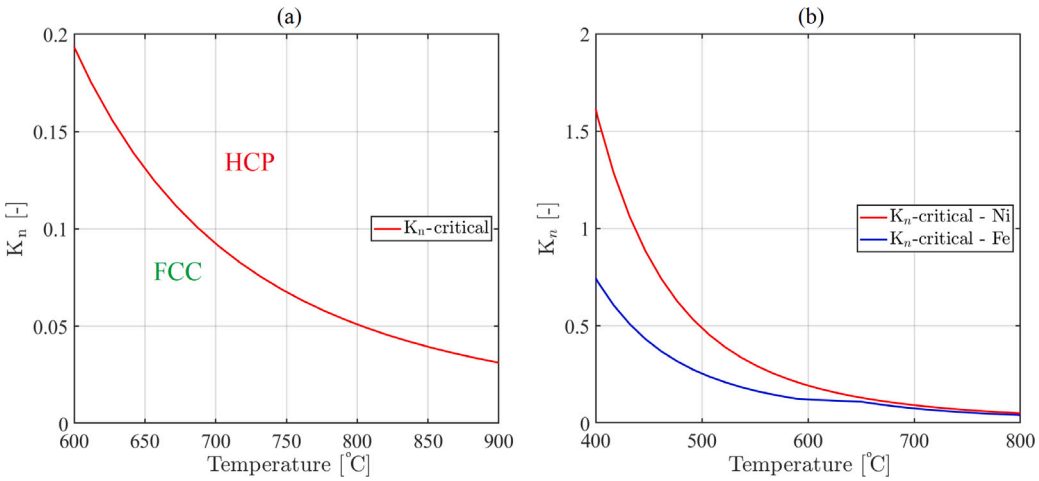

Fig. 2. Variation of critical nitriding potential ($K_{n,cr}$) by temperature for (a) Ni and (b) Ni and Fe.

Table 1
Cell polarization model governing equations.

Description	Governing equation	Eq.
Cell voltage [43]	$V_{cell} = E_{eq} - (\eta_{act,an} + \eta_{act,ca} + \eta_{conc,an} + \eta_{conc,ca} + \eta_{ohm})$	(5)
Open-circuit voltage (OCV) [43]	$E_{eq} = \frac{\Delta G}{nF} + \frac{RT}{nF} ln(\frac{P_{H_2} P_{O_2}^{0.5}}{P_{H_2O} P_{ref}^{0.5}})$	(6)
Butler–Volmer (BV) [44]	$J = J_{0,an/ca}[exp(-\alpha_{an/ca} \frac{nF\eta_{act,an/ca}}{RT}) -$ $exp(-(1-\alpha_{an/ca}) \frac{nF\eta_{act,an/ca}}{RT})]$	(7)
Anode exchange current density [44]	$J_{0,an} = \gamma_{an} (\frac{P_{H_2}}{P_{ref}})^a (\frac{P_{H_2O}}{P_{ref}})^b exp(\frac{-E_{act,an}}{RT})$	(8)
Cathode exchange current density [44]	$J_{0,ca} = \gamma_{ca} (\frac{P_{O_2}}{P_{ref}})^m exp(\frac{-E_{act,ca}}{RT})$	(9)
Anode concentration overpotential [45]	$\eta_{conc,an} = \frac{RT}{n_{e,a}F} ln(\frac{x_{H_2}^{ei} x_{H_2O}^{ee}}{x_{H_2}^{ee} x_{H_2O}^{ei}})$	(10)
Cathode concentration overpotential [45]	$\eta_{conc,ca} = \frac{RT}{n_{e,c}F} ln((\frac{x_{O_2}^{ei}}{x_{O_2}^{ee}})^{0.5})$	(11)
Ohmic overpotential [44]	$\eta_{ohm} = J \frac{T}{B_{ohm}} exp(\frac{E_{act,ohm}}{RT})$	(12)
Dusty-gas model (DGM) fluxes [46]	$\frac{N_1}{D_{1K}^{eff}} + \frac{x_2 N_1 - x_1 N_2}{D_{12}^{eff}} = -\frac{1}{RT}(p\Delta x_1 + x_1 \Delta p + x_2 \Delta p) \frac{kp}{D_{1K}^{eff} \mu}$	(13)
	$\frac{N_2}{D_{2K}^{eff}} + \frac{x_1 N_2 - x_2 N_1}{D_{12}^{eff}} = -\frac{1}{RT}(p\Delta x_2 + x_1 \Delta p + x_2 \Delta p) \frac{kp}{D_{2K}^{eff} \mu}$	(14)
Binary diffusion coefficient [47]	$D_{ij} = \frac{0.00143T^{1.75}}{PM_{ij}^{0.5}(V_i^{1/3} + V_j^{1/3})^2}$; $M_{ij} = \frac{2}{M_i^{-1} + M_j^{-1}}$	(15)
Knudsen diffusion coefficient	$D_{ik} = \frac{d_p}{3} \sqrt{\frac{8RT}{\pi M_i}}$	(16)
Effective diffusion coefficient	$D_{ij}^{eff,an/ca} = k_{D,eff}^{an/ca} D_{ij}^{an/ca}$	(17)
Inlet molar flow rate	$\dot{n}_{in} = Q_{in} \frac{p}{RT}$	(18)
Species molar flow rate at the inlet	$\dot{n}_{in,i/j} = x_{in,i/j} \dot{n}_{in}$	(19)
Species molar flow rate at the outlet	$\dot{n}_{out,i/j} = \dot{n}_{in,i/j} + \dot{n}_{react,i/j}$	(20)
Species mole fraction at the outlet	$x_{out,i/j} = \frac{\dot{n}_{out,i/j}}{\dot{n}_{out,i} + \dot{n}_{out,j}}$	(21)

ferrite (LSCF) or LSFC-Gadolinium-Doped Ceria (CGO) [42], which are used in high temperature cells. LSC has a very high electronic conductivity. However, the thermal expansion coefficient for LSC is higher than LSFC and other cell layers, making LSC less favorable to operate at higher temperatures due to the larger discrepancy of thermal expansions leading to higher thermal stresses. Also, the barrier layer for LT cells is thinner than HT cells, which leads to lower resistance.

It should be noted that the modeling in this section has been conducted to identify the parameters representing various cell characteristics. At the stack level, these parameters are transferred to the 3D model of the stack. The equations for the cell-level modeling are presented in Table 1. A detailed explanation of these equations is presented in our previous studies [48,49].

The governing equations presented in Table 1 have 13 free parameters, which can be adjusted by adapting the model with a large number of independent experimental measurements, where the conditions are chosen such that all parameters can be identified. B_{ohm} and $E_{act,ohm}$ are initially calculated using electrochemical impedance spectroscopy data to reduce the number of unknowns to 11 parameters. The remaining 11 parameters are calculated to obtain the best validation with the available experimental data. All of the 13 parameters for low and high temperature cell technologies are represented in Table 2. The validation of the developed model at the cell level is represented for low and high temperature cells in Appendix B and Ref. [41], respectively.

In our recent study [41], a detailed 3D model of a direct and pre-cracked ammonia-fueled SOFC at the cell level is presented for the high temperature cells. The developed model showed a good agreement with the experimental data. The validation of the detailed cell level model is presented in Appendix C.

Table 2
Values of parameters for cell model obtained from validation with experimental data. The first row for each parameter represents the value for the high temperature cells and the second row represents the values for the low temperature cells.

Parameter	value	Description
$\gamma_{0,an}$	8.998×10^6	Constant of the prefactor used for the anode exchange current density [A/m^2 K]
	1.949×10^6	
$\gamma_{0,ca}$	2.434×10^8	Constant of the prefactor used for the cathode exchange current density [A/m^2 K]
	7.837×10^8	
$E_{act,an}$	1.206×10^5	Activation energy used for the anode exchange current density [J/mol]
	1.065×10^5	
$E_{act,ca}$	1.481×10^5	Activation energy used for the cathode exchange current density [J/mol]
	5.122×10^4	
α_{an}	0.772	Charge transfer coefficient of the anode reaction [−]
	0.560	
α_{ca}	0.830	Charge transfer coefficient of the cathode reaction [−]
	0.672	
a	−0.058	Power of the hydrogen partial pressure used for the anode exchange current density [−]
	−0.089	
b	0.488	Power of the steam partial pressure used for the cathode exchange current density [−]
	0.381	
m	0.182	Power of the oxygen partial pressure used for the cathode exchange current density [−]
	0.196	
$k^{an}_{D,eff}$	0.169	Correction factor for the diffusion coefficients of the species in the anode porous media
	0.21	
$k^{ca}_{D,eff}$	0.199	Correction factor for the diffusion coefficients of the species in the cathode porous media
	0.21	
B_{ohm}	7.825×10^{11}	Material specific constant used for the ohmic overpotential [SK/m^2]
	7.294×10^{12}	
$E_{act,ohm}$	8.002×10^4	Activation energy used for the ohmic overpotential [J/mol]
	9.238×10^4	

2.4. Stack level modeling

In the current study, 3D simulations are conducted using COMSOL Multiphysics 6.1 to investigate the performance of an ammonia-fueled SOFC stack. Fig. 3 illustrates the 3D geometry of the modeled SOFC stack, the computational mesh, and the inlet and outlet of the air and fuel streams. The modeling domain encompasses various components, including the active area, headers, sealing domains, and manifolds. The SOFC stack model employed in this study utilizes a homogenization approach, where the detailed geometric response of the actual structure is represented through effective material properties of a homogeneous volume, e.g. average thermal conductivities in different directions of the layered structure. In this manner, the transport of mass, momentum, species, charges, and heat as well as the electro-chemical reactions within the stack can be described [43]. It is currently not possible to homogenize the non-linear Navier–Stokes equations for the turbulent and laminar free flow in the manifolds by homogenization. Thus, here a coupling between the free flow and the homogenized equations describing the headers and repeating units inside the stack is employed [48,50].

The method also allows for describing localized effects, by representing the original structure of the stack and applying the homogenized average parameters as boundary conditions. An example of this is localized mechanical failures within the repeating unit of the stack [51], as well as the distribution of the localized ammonia cracking within the cells everywhere in the stack [11]. In some cases this submodel can be conducted once and for all, and the localized parameters can be achieved in the homogenized model, which is the case for both ammonia cracking and the overpotential distribution inside the electrodes [11]. For further description of the homogenization approach, please refer to previous works on the method.

The reason for using the homogenization method is that it is far more computationally efficient than explicitly representing all the repeating geometrical features of the stack, as the number of finite elements is heavily reduced and simulation load is decreased by at least a factor of 100 [48]. This makes it possible to describe e.g. degradation at different locations within the stack throughout the lifetime of the stack [48] or as in this case, makes it is feasible to simulate the entire stack together with the remaining system.

Table 3
Governing equations for the stack model.

Description	Governing equation	Eq.
Mass	$\nabla.(\rho\mathbf{u}) = S_m$	(22)
Momentum	$\rho(\mathbf{u}.\nabla)\mathbf{u} = -\nabla p + \mu\nabla^2\mathbf{u}$	(23)
Species	$\nabla.(-\rho w_i \sum D_{ij}\nabla w_j) + \rho(\mathbf{u}.\nabla)w_i = S_i$	(24)
Charge	$\nabla.(-\sigma\nabla V + J_e) = S_j$	(25)
Heat	$(\rho c_p)_{eff}\mathbf{u}.\nabla T + \nabla.(-k_{eff}\nabla T) = S_T$	(26)

The modeling domain corresponds to the right half of the stack, with a symmetry boundary condition applied to the middle surface in the x-direction 3c. The computational mesh is refined at the inlet region of the active layer and inlet header to capture the large gradients of parameters due to the high cracking rate of ammonia at the inlet (Fig. 3c). The SOFC stack model utilizes a computational mesh comprising 81 thousand finite elements, resulting in approximately 1.1 million degrees of freedom (DOF).

The governing transport equations of mass, momentum, species, charges, and heat are used in the developed model [43,49]. The governing equations for the SOFC stack modeling are given in Table 3. For the inlets of air and fuel, the fully developed flow boundary condition is considered.

In previous study [48,50], it was demonstrated that the homogenized model for stack simulation adeptly reproduces the experimental data acquired from an 18-cell FZJ Mark-F SOFC stack [52] operating with hydrogen fuel. The validation of the homogenized model for hydrogen-fueled SOFC stack is also presented in Appendix D. Since there is a scarcity of experimental data available for direct ammonia-fueled SOFC stacks, the current developed model for SOFC stacks has not been validated specifically for ammonia fuel. However, in our recent study [41], the same numerical models and equations as the current study are utilized in a developed detailed 3D model of a direct and pre-cracked ammonia-fueled SOFC at the cell level. The electrochemical reactions relied only on reaction kinetics of hydrogen, considering ammonia cracking kinetics. The model was shown to provide rather good agreement with experimental data under a broad range of operating conditions with ammonia as a fuel. This proves the validity of the developed utilized numerical models for the simulation of ammonia-fueled SOFCs.

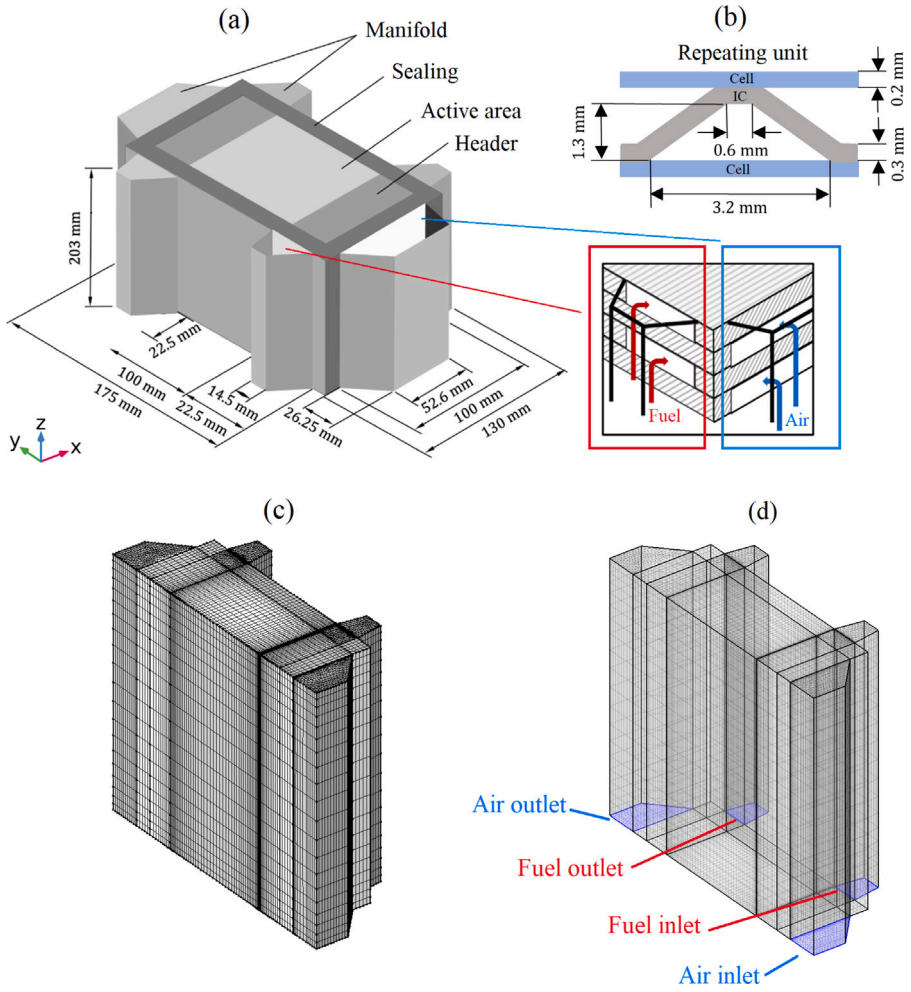

Fig. 3. Schematic of the (a) stack configuration and (b) repeating unit. The computational mesh is depicted in (c) and the inlet and outlet of the air and fuel streams are shown in (d).

2.5. System level modeling

In the present study, a novel approach is employed for system modeling. In this approach, the detailed 3D modeling of the SOFC stack is integrated with system modeling, and all the pertinent equations are solved simultaneously within the COMSOL Multiphysics software. Using this approach, the influence of system-level complexities is imposed on the boundaries of the 3D stack model, while the system model benefits from the precision of the 3D stack model. Eventually, this will also enable the co-simulation of transients in the system and stack, but this is outside the scope of the current work.

This study follows a two-step process for system design and analysis. Initially, the system is designed using Engineering Equation Solver (EES) or MATLAB, employing system-level thermodynamic equations. Subsequently, the designed system is transferred to the COMSOL Multiphysics software, where all system equations are solved together with detailed 3D multiphysics modeling of the SOFC stack in a single model. The purpose is also to validate the integrated approach with the conventional approach. A steady-state operating condition is assumed for each component and the entire ammonia-fueled SOFC system. Mass and energy conservation equations are formulated as follows in COMSOL for each system component:

$$\sum \dot{n}_i M_i = \sum \dot{n}_o M_o \tag{27}$$

$$\sum \dot{n}_i h_i + \dot{Q}_{cv} = \sum \dot{n}_o h_o + \dot{W}_{cv} \tag{28}$$

where $\dot{n}$, M, h, $\dot{Q}$, and $\dot{W}$ are mole flow rate, molar mass, specific enthalpy, heat transfer rate, and power, respectively. Indexes i, o, and cv refer to inlet, outlet, and control volume, respectively.

The stack power (P_{stack}) and system power (P_{system}) are calculated using the following equations:

$$P_{stack} = V \times I \tag{29}$$

$$P_{system} = P_{stack} - P_{loss} \tag{30}$$

where V and I are the voltage and current of the SOFC stack and P_{loss} is the consumed power (power losses) in the system for the fuel and air supply.

The schematic of the ammonia-fueled system is presented in Fig. 4. The regulation of the ratio between pre-cracked ammonia and non-cracked ammonia supplied to the SOFC stack is achieved through the utilization of two valves within the system. Therefore, valves 1 and 2 specify how much of the inlet ammonia undergoes the internal cracking inside the SOFC stack and how much cracks in the external cracker as shown in Fig. 4.

The operating conditions and assumptions for different components in the system are presented in Table 4. A maximum temperature variation of 100 °C is permitted within the stack constraints imposed by the materials related to thermal stresses resulting in mechanical failures. Due to the high pressure in the ammonia storage tank and the low flow rate of fuel, there are no blowers on the fuel side of the system. The magnitude of the pressure drop in the SOFC stack is obtained from

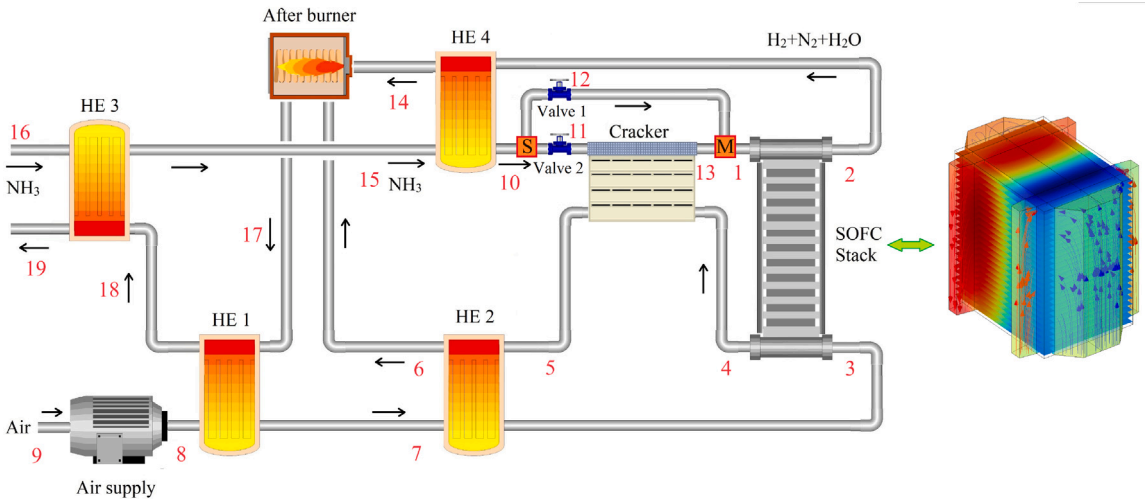

Fig. 4. Schematic of the designed system for ammonia-fueled SOFC. Heat exchangers are referred as HE in the schematic. Red numbers specify different states in the system.

Table 4
Operating conditions and assumption for the parameters used in the system modeling.

Parameter	Value [unit]
SOFC fuel utilization factor	70 [%]
SOFC operating current density	0.25 [A/cm^2]
Maximum temperature variation within the SOFC stack	100 [°C]
Maximum effectiveness of heat exchangers	90 [%]
Air compressor isentropic efficiency	85 [%]
Air and fuel inlet temperature	From 3D model
Air and fuel outlet temperature	From 3D model
Pressure drop within the SOFC stack on the air side	From 3D model
Pressure drop within the air heat exchangers on one side	10 [mbar]
Pressure drop within the afterburner on the air side	10 [mbar]
Pressure drop within the cracker on the air side	10 [mbar]

Table 5
Energy conservation equations of the main components of the system. For state numbers see Fig. 4.

System component	Equation
Air supply (compressor)	$\dot{W}_{COMP} = \dot{n}_9(h_9 - h_8)$
Heat exchanger 1 (HE 1)	$\dot{n}_8(h_7 - h_8) = \dot{n}_{17}(h_{17} - h_{18})$
Heat exchanger 2 (HE 2)	$\dot{n}_7(h_3 - h_7) = \dot{n}_5(h_5 - h_6)$
Heat exchanger 3 (HE 3)	$\dot{n}_{16}(h_{15} - h_{16}) = \dot{n}_{18}(h_{18} - h_{19})$
Heat exchanger 4 (HE 4)	$\dot{n}_{15}(h_{15} - h_{10}) = \dot{n}_2(h_2 - h_{14})$
Cracker	$\dot{n}_4(h_4 - h_5) = \dot{n}_{13}h_{13} - \dot{n}_{11}h_{11}$
After burner	$\dot{n}_{14}h_{14} + \dot{n}_{15}h_{15} = \dot{n}_{17}h_{17}$
Splitter (S)	$\dot{n}_{10}h_{10} = \dot{n}_{11}h_{11} + \dot{n}_{12}h_{12}$
Mixture (M)	$\dot{n}_{12}h_{12} + \dot{n}_{13}h_{13} = \dot{n}_1h_1$

the 3D multiphysics model. For the other components of the system, the assumed pressure drops in the air side of the system are presented in Table 4 for the case with the lowest air flow rate. It is assumed that by increasing the air flow rate for other cases, the pressure drops will increase linearly.

2.6. Coupling different levels of modeling

In this section, the coupling and relations between different levels of modeling are explained. Ammonia cracking is not happening through the whole length of the fuel electrode as shown in Ref. [41] and schematically shown in Fig. 1a. Therefore, it is important to accurately capture the ammonia penetration in the fuel electrode to have an accurate connection between the cell level and stack level modeling. In this regard, ammonia penetration depth in the fuel electrode (h_{NH_3}) is defined as follows [11]:

$$h_{NH_3} = \sqrt{\frac{\rho D w^{ch}_{NH_3}}{R^{Ni-YSZ}_{crack} M_{NH_3}}} \tag{31}$$

where, ρ is the density, D is the diffusion coefficient, and w is the mass fraction. The detailed explanation and derivation of this equation are presented in Ref. [11]. After finding the correct penetration and cracking of ammonia in a cell inside the stack, the rest of the physics are solved similarly to a hydrogen-fueled SOFC [43].

For the connection between stack level and system level, it should be mentioned that the stack model represents the core of the model. All of the underlying physics within the stack including ammonia cracking, transport of mass, momentum, species, charges, and heat as well as the electrochemical reactions within the stack are solved in the 3D stack model. For each of the system components mass and energy balance equations (Eqs. (27) and (28)) have been formulated and added as additional ordinary differential equations in COMSOL. This is the case for all the system components such as the compressor, external ammonia cracker, air compressor, and heat exchangers. These equations are included as Global ODE and DAE interfaces in the COMSOL model and are solved simultaneously with the 3D model equations.

The air and fuel side flow rates of the SOFC stack as well as stack inlet temperature are calculated based on the stack operating conditions and assumptions (such as maximum 100 °C temperature variation) that are considered for safe operation of the stack. With the same inlet fuel flow rate for all cases, the operating conditions will affect the inlet temperature, air flow rate, and consequently, pressure drops (see Table 6). Having the required air flow rate and pressure drops, the consumed power in the air supply unit is calculated. Additionally, the heat exchangers are designed to ensure the required inlet temperature of the SOFC stack, using the SOFC stack outlet temperature obtained from the 3D model of the stack. The energy conservation equations of the main components of the system that are added in the COMSOL model are represented in Table 5.

3. Results and discussion

In this section, the results of the stack/system model are presented. The results section is organized as follows:

- Section 3.1: describes the different studied cases operating conditions obtained from the coupling of 3D multiphysics model and system model.
- Section 3.2: studies the effects of fuel composition and operating temperature on the SOFC stack performance.

Table 6
Operating conditions for low and high temperature (LT and HT) cases. LT-L and LT-H refer to cases operating under low temperature conditions (600–700 °C) with the cells designed for low and high temperature operation, respectively.

Case ID	Temperature range [°C]	Pre-cracking ratio [%]	Inlet temperature [°C]	Air flow rate [g/s] LT-H/LT-L	Pressure drop air side of stack [mbar] LT-H/LT-L
LT-00% crack	600–700	0	618	2.55/1.20	2.72/1.23
LT-20% crack	600–700	20	609	2.90/1.65	3.13/1.72
LT-40% crack	600–700	40	605	3.40/2.15	3.74/2.29
LT-60% crack	600–700	60	604	3.90/2.73	4.36/2.97
LT-80% crack	600–700	80	602	4.40/3.30	5.00/3.66
LT-100% crack	600–700	100	600	5.00/3.80	5.77/4.28
HT-00% crack	700–800	0	755	1.80	2.27
HT-20% crack	700–800	20	732	2.00	2.52
HT-40% crack	700–800	40	713	2.20	2.78
HT-60% crack	700–800	60	705	2.65	3.40
HT-80% crack	700–800	80	703	3.20	4.19
HT-100% crack	700–800	100	700	3.70	4.91

- Section 3.3: investigates the influences of fuel composition and operating temperature on nitriding potential.
- Section 3.4: indicates the effects of fuel composition and operating temperature on system performance.

3.1. Description of the studied cases and coupling of 3D multiphysics model and system model

This section provides a detailed description of the operating conditions for all the cases analyzed in this study. Furthermore, the value of the direct coupling of the different levels of models is shown.

3.1.1. Operating conditions

Considering the constraints imposed by the materials related to thermal stresses, typically, a specific degree of temperature variation is permissible within the SOFC stacks. Hence, in the present study, a maximum temperature variation of 100 °C is permitted within the stack.

As mentioned, two different cell technologies designed for low and high temperature operation are investigated here. These two different cell types are analyzed at two different temperature ranges, i.e. 600–700 °C, referred to as low temperature (LT), and 700–800 °C, referred to as high temperature (HT). It is worth mentioning that these temperature ranges are considered reasonable based on the information provided by various SOFC stack manufacturers. For each cell technology, various ratios of ammonia pre-cracking including 0%, 20%, 40%, 60%, 80%, and 100% are considered. This will be used later on to show the minimum safe limit for pre-cracking with respect to nitriding. An overview of the investigated operating conditions for different cases is presented in Table 6.

In the experimental and numerical investigations on the SOFCs, usually the same kind of cells are examined under various operating temperatures. However, it would not be optimal to operate either cell technology in the other temperature regime. To have an understanding of the influence of using the same cell technology in different temperature regimes on the system-level results, the high temperature cell technology has also studied at low temperature. The cases operating under low temperature with the cells designed for low temperature operation are referred to as LT-L and the cases with cells designed for high temperature operation are referred to as LT-H.

The system equations leave two open parameters, which can be used for defining the operating conditions. These are here chosen to be the stack inlet temperature and the air flow rate. These two parameters are adjusted for each system in Table 6 to achieve the maximum allowable temperature span over the stack (100 °C). The stack inlet temperature affects the minimum temperature of the stack. It should be controlled and adjusted in a way that the minimum temperature in the stack does not drop below the minimum allowable temperature in the active area, due to the endothermic cracking of ammonia. On the other hand, the air flow rate affects the maximum temperature of the stack by cooling down the stack to the desired temperature range.

3.1.2. Coupling of 3D multiphysics model and system model

As explained in Section 3.1.1, stack inlet temperature and air flow rate are adjusted for all the systems to achieve the maximum allowable temperature span of 100 °C within the stack. The result of this can be found for the different cases in Table 6.

From Table 6, some noteworthy observations can be made regarding the different cases. The first one is the inlet temperature of the SOFC stack for low and high temperature cases. All inlet temperatures with ammonia partially present in the fuel are higher than the desired minimum temperature inside the stack, as the cracking of the ammonia introduces local cooling inside the stack. For the LT cases (600–700 °C), the inlet temperature is closer to the lower bound of the temperature range (600 °C) than that for the HT cases (700 °C). For example, according to Table 6, the inlet temperature of LT case without pre-cracking (LT-00% crack) is only 18 °C higher than 600 °C (i.e. 618 °C), while this temperature difference is 55 °C (i.e. 755 °C) for its HT counterpart (HT-00% crack). The reason behind this result is the lower cracking rate of ammonia in the LT cases compared to the HT cases. This results in a smaller reduction in local temperature at the entry over the active area for the LT cases, as shown in Fig. 5 in comparison to the HT ones.

Distribution of temperature inside the stack for the cases with different ammonia pre-cracking ratios are shown in Fig. 6. These figures are presented for high temperature (HT) cells (700–800 °C) and for the center line (line 4 in Fig. 5c) and the bottom line (line 7 in Fig. 5c). It is here chosen to show the results for the HT cells in Fig. 6 due to large variation in temperature distribution as a result of more intense localized ammonia cracking and resulting temperature reduction. The center line and bottom line are selected as they represent the maximum and minimum temperature inside the stack, respectively.

Fig. 6a shows the distribution of temperature on the bottom line which is constant in the air inlet channel. This is because a uniform temperature profile is considered for inlet streams. Then, the temperature suddenly drops due to the endothermic cooling of ammonia and high conductive heat transfer in the metal parts of the stack (see different parts of SOFC stack in Fig. 3). From the start of the active area at −50 mm, the temperature starts to gradually increase due to heat formation in the active area (see Fig. 7). An increase and decrease can be seen at the end of the temperature profile as shown in Fig. 6a. This part of the temperature profile shows the air flow temperature in the outlet air manifold.

It is worth mentioning that as can be seen in Fig. 6, despite the lower inlet temperature for the cases with higher pre-cracking ratios, the average temperature of the active area is higher. This will affect the SOFC stack power production (see Section 3.4).

Another observation from Table 6 is that, for cases with similar pre-cracking ratios, the LT-H cases require a higher air flow rate than LT-L and HT cases to cool down the stack to the desired maximum temperature difference of 100 °C. This is to be expected as the internal

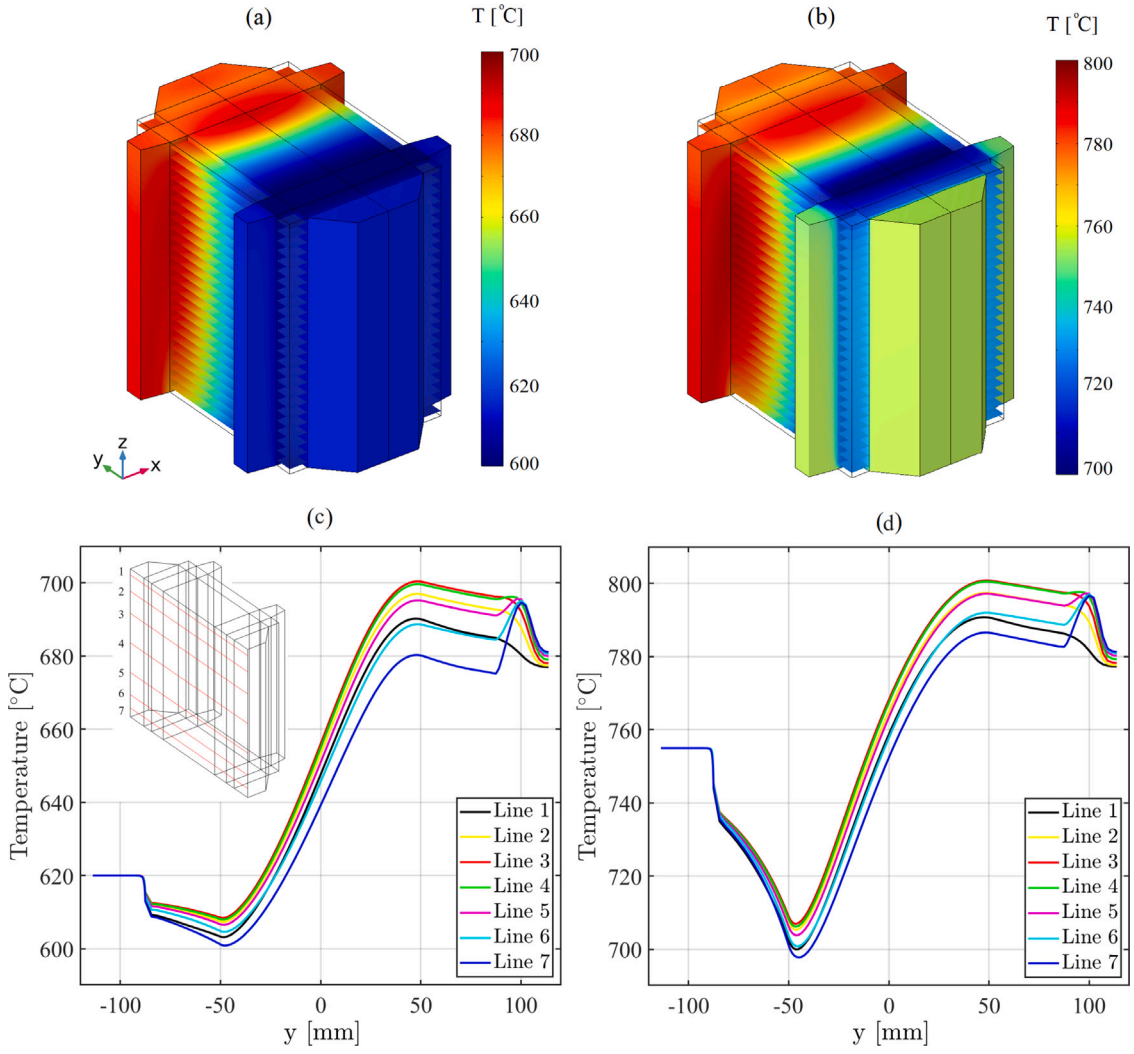

Fig. 5. Distribution of temperature inside the stack for the cases with no ammonia pre-cracking under (a) and (c) low temperature (LT) condition (600–700 °C), (b) and (d) high temperature (HT) condition (700–800 °C). Location of probe lines is shown in Fig. 5c.

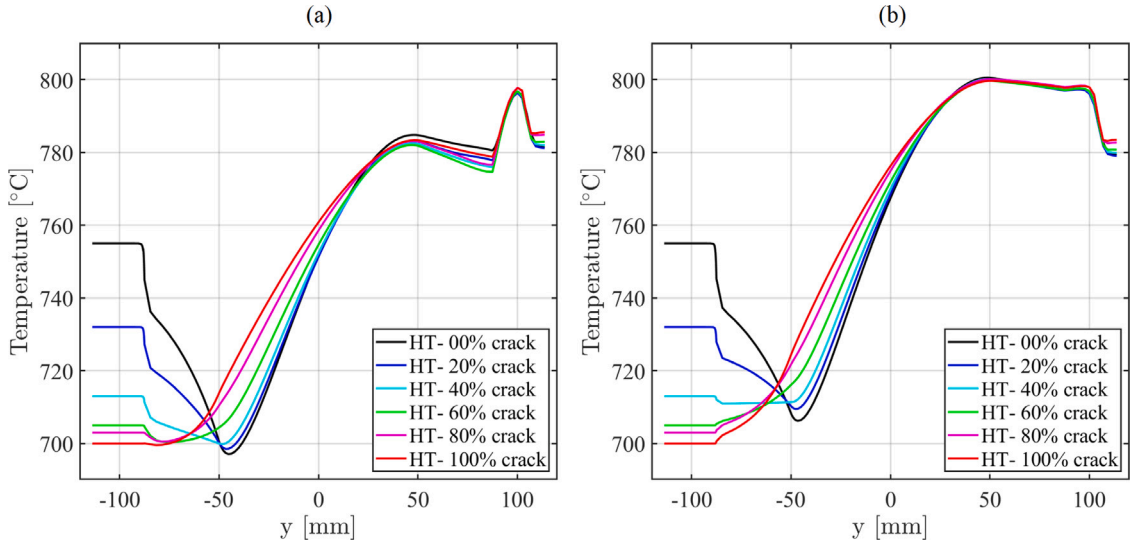

Fig. 6. Distribution of temperature inside the SOFC stack for the cases with different ammonia pre-cracking ratios for high temperature (HT) cell (700–800 °C) (a) at the center line (line 4 in Fig. 5c) and (b) at the bottom line (line 7 in Fig. 5c).

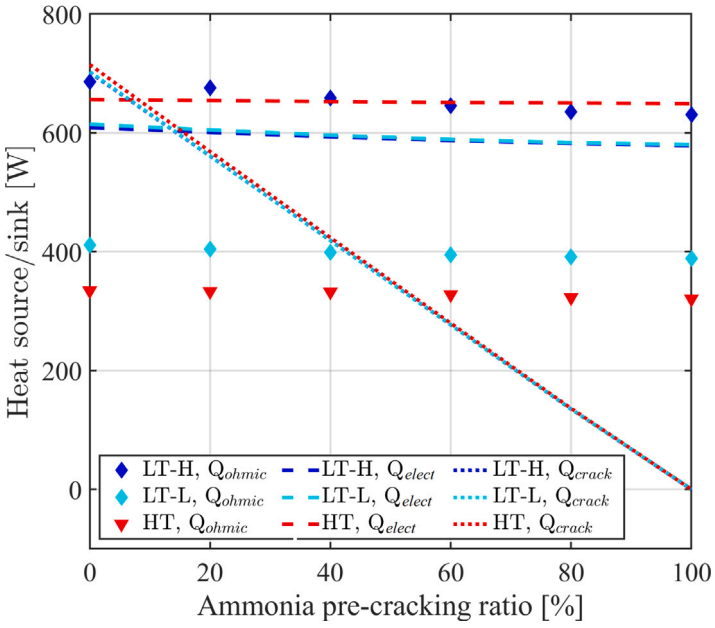

Fig. 7. Variation of different heat sources/sinks by changing the operating temperature and pre-cracking ratio of ammonia fuel. LT-L and LT-H refer to cases operating under low temperature conditions (600–700 °C) with the cells designed for low and high temperature operation, respectively.

resistance of the high temperature cells is higher at lower temperatures. This can also be seen in Fig. 7, which illustrates the various heat sources and sinks within the SOFC stack for different ammonia pre-cracking ratios. The heat sources in the system consist of ohmic heat (Q_{ohmic}) and electrochemical reaction heat (Q_{elect}), while the ammonia cracking heat (Q_{crack}) serves as a heat sink resulting from the endothermic cracking of ammonia.

It is clear that for the high temperature cells (with thicker electrolyte), especially the ohmic heat source, Q_{ohmic}, is larger than in the other cases, where the cells are operating in their desired range. Further explanations regarding the ASRs will be provided in the subsequent section. On the other hand, Q_{elect} is slightly higher for the HT cases. Q_{crack} is similar for all cases as the inlet molar flow rate of ammonia is the same for all cases and enthalpy variation during cracking (ΔH in Eq. (2)) is not highly dependent on the operating temperature. In summary, the combined effect of the aforementioned heat sources and sinks results in higher heat generation within the SOFC stack in LT-H cases compared to HT and LT-L cases. Consequently, a higher air flow rate is required to remove the excess heat from the SOFC stack in the LT-H cases.

Furthermore, by increasing the pre-cracking ratio, Q_{crack} is reduced because a portion of the ammonia is already cracked outside the SOFC stack in the external cracker (see Fig. 4). According to Table 6, increasing the ammonia pre-cracking ratio results in a twofold and threefold increase in the required air flow rate for high-temperature cell technology (HT and LT-H) and low-temperature cell technology (LT-L), respectively.

3.2. Effects of fuel composition and operating temperature on stack performance

In this section, the performance of SOFC stack fueled by direct ammonia and partially pre-cracked ammonia is compared and examined. Initially, the analysis focuses on the distribution of species, followed by an examination of the current density distribution, and finally, an investigation of the area specific resistances (ASRs).

3.2.1. Distribution of species

Fig. 8 shows the distribution of ammonia and hydrogen mole fractions in the active area of the SOFC stack along the center line of the stack for low temperature (LT) and high temperature (HT) cases. As a result of the lower cracking rate of ammonia in the LT cases (LT-L and LT-H), ammonia survives and penetrates further inside the SOFC stack compared to HT cases. As evident from Fig. 8, ammonia demonstrates a penetration depth of approximately 75 mm (out of 100 mm) within the active area of the SOFC stack in the LT-H and LT-L cases. On the other hand, ammonia only survives the first 25 mm of the active area in HT cases.

All of the hydrogen in direct ammonia-fueled systems (i.e., 00% pre-crack) is generated through ammonia internal cracking, while only a portion of it is produced in pre-cracked cases by internal cracking of ammonia inside the SOFC stack. In the HT cases, as ammonia undergoes cracking within the initial 25 mm of the active area, a large amount of hydrogen is available even within the first quarter of the active area. In the LT cases (LT-L and LT-H), due to the lower cracking rate of ammonia and continuous consumption of ammonia along the active area of the SOFC stack, the maximum amount of hydrogen is considerably lower than that in the HT cases.

Fig. 8 also shows that the consumption rate of hydrogen for LT-L cases is slightly higher than that for the LT-H cases (see hydrogen molar fraction at y = 0 mm). This leads to lower local hydrogen concentration which results in a higher ammonia cracking rate (see Eq. (1)). Therefore, ammonia penetrates slightly less in LT-L cases (~72 mm) compared to LT-H cases (~75 mm).

3.2.2. Current density distribution

Fig. 9 depicts the current density distribution in the active area of the SOFC stack for LT-L, LT-H and HT cases under various ammonia pre-cracking ratios. In the LT-H and LT-L cases, the current density increases gradually from the start of the active area (y = −50 mm) and reaches a maximum value close to the end of the active area (y = 50 mm) and then decreases. Furthermore, by increasing the ratio of ammonia pre-cracking, the current density distribution becomes more uniform, especially in the LT-H cases. On the other hand, the current density increases initially and then decreases gradually in the HT cases. Moreover, increasing the ammonia pre-cracking rate reduces

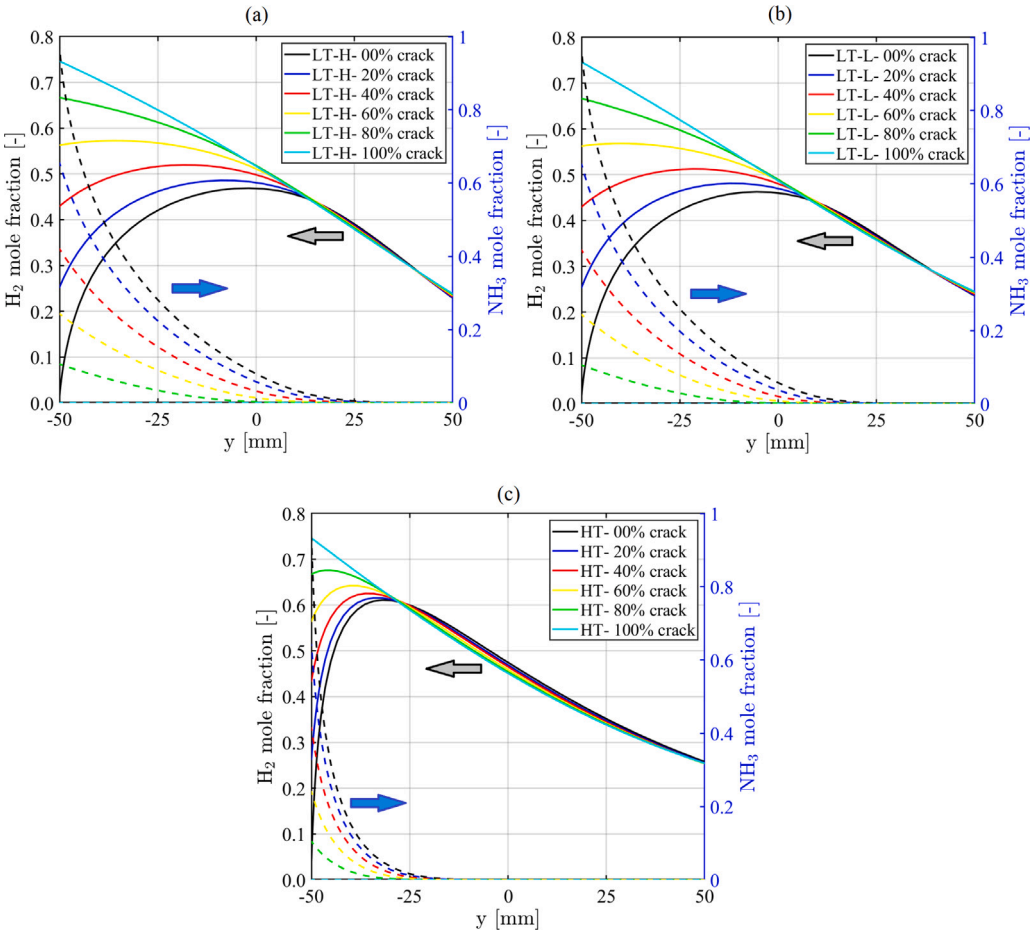

Fig. 8. Distribution of ammonia (dashed lines) and hydrogen (solid lines) mole fractions in the active area of the SOFC stack on the center line for (a) low temperature (LT) condition (600–700 °C) with cells designed for high temperature (LT-H), (b) low temperature (LT) condition with cells designed for low temperature (LT-L), and (c) high temperature (HT) condition (700–800 °C) under various ammonia pre-cracking ratios.

the uniformity of the current density distribution along the active area of the SOFC stack.

The distribution of area specific resistances (ASRs) in the active area of the SOFC stack on the center line is presented in Fig. 9c for cases without cracking. As can be seen, for the LT-H cases there is a large variation in the local distribution of ASR from the start of the active area to the end. This leads to higher current densities at the end with much lower ASR compared to the start of the SOFC. On the other hand, in the HT cases, the ASR does not vary considerably from the start of the active area to the end. Therefore, due to higher hydrogen molar fractions at the start, the current density is also higher at the start of the active area for the HT cases. Various ASRs will be elaborated in the following subsection.

3.2.3. Average area specific resistances

The average ASRs, including the ASRs related to activation (ASR_{act}), ohmic (ASR_{ohm}), and concentration (ASR_{conc}) overpotentials [43] in the active area of the SOFC stack, are depicted in Fig. 10 for various ammonia pre-cracking ratios. As can be seen, the magnitude of the ASR_{conc} for all LT and HT cases is negligible. It is important to notice that because of the relatively low fuel utilization (70%), fuel starvation is not present and the concentration overpotential remains at a moderate level. Fuel starvation could become a problem if ammonia was not cracked fast enough over the cells. It should be mentioned that a constant value of 0.2 Ω m^2 is considered as contact resistance for all of the cases that are added to the ASR_{ohm} in Fig. 10.

In HT cases, the elevated operating temperature results in higher thermally activated electrochemical reactions, leading to an increased reaction rate. The higher temperature also leads to faster charge transfer and the ASR_{act} is considerably lower in HT cases compared to LT-H cases. Furthermore, the ASR_{act} is reduced by increasing the ammonia pre-cracking ratio for all cases, as this raises the average temperature of the active area. For example, the average temperature of the active area is around 756 and 769 °C for the no pre-cracking (HT-00%crack) and the completely pre-cracked (HT-100%crack) cases, respectively. Even though both cases have the same range of operating temperatures i.e. 700–800 °C, the endothermic cracking of ammonia reduces the average temperature of the active area.

The ASR_{ohm} also reduces by increasing the operating temperature as the higher temperatures facilitate better ionic mobility within the electrolyte, reducing the resistance to ion movement. This leads to lower ASR_{ohm} for HT cases compared to LT cases. The ASR_{ohm} of LT-L cases is also much lower than LT-H cases as the electrolyte layer is thinner for the cells designed for low temperature operation which leads to lower ASR_{ohm} (check Eq. Table (12) and values of B_{ohm} and $E_{act,ohm}$ in Table 2 for different cells). The ASR_{ohm} decreases with an increase in the ammonia pre-cracking ratio, primarily because of the higher average temperature in the active area of the SOFC stack.

3.3. Effects of fuel composition and operating temperature on nitriding

In addition to its numerous advantages, direct ammonia feeding in SOFCs also comes with certain drawbacks. Ni nitriding in the anode layers as one of the main challenges in the direct ammonia-fueled SOFCs is investigated here under various operating conditions. A qualitative validation of the utilized modeling method for Ni nitriding potential

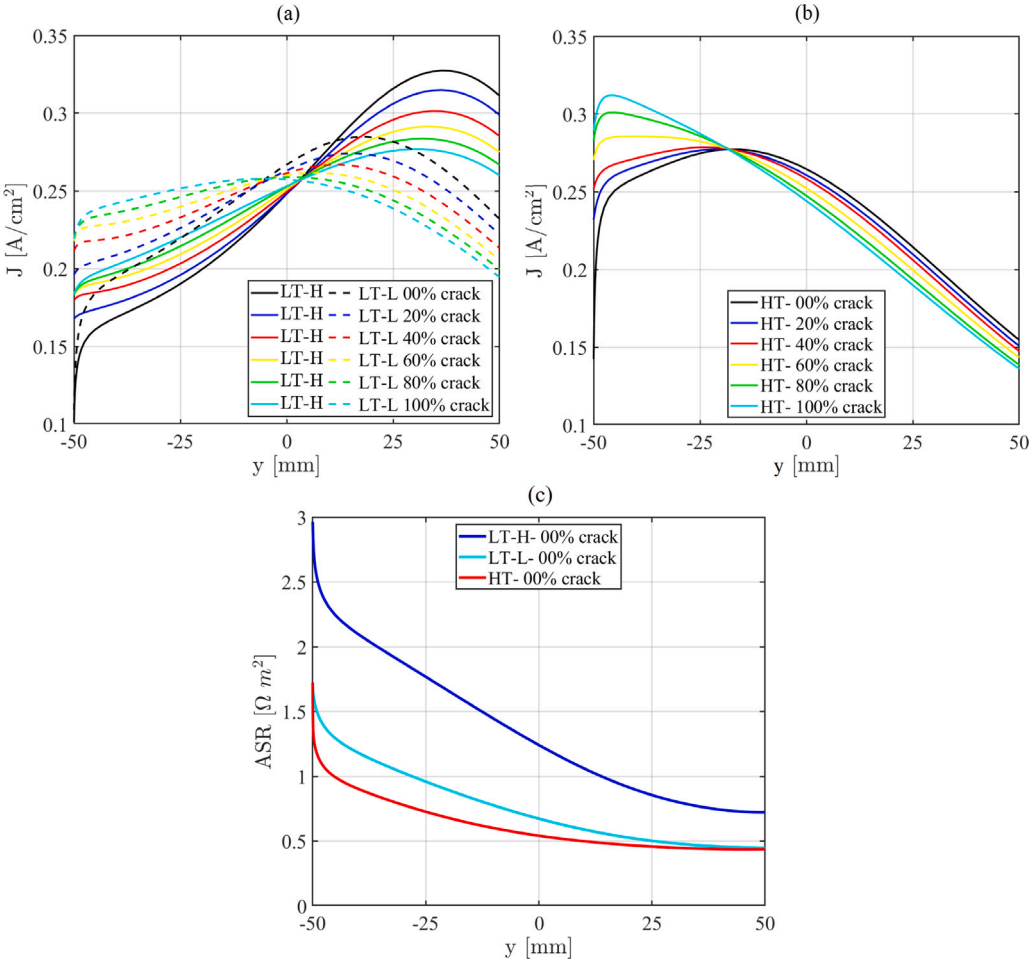

Fig. 9. Distribution of current density in the active area of the SOFC stack on the center line for (a) low temperature (LT) condition (600–700 °C) - solid lines for LT-H and dotted lines for LT-L cases and (b) high temperature (HT) condition (700–800 °C) under various ammonia pre-cracking ratios. (c) Distribution of ASRs in the active area of the SOFC stack on the center line for cases without pre-cracking.

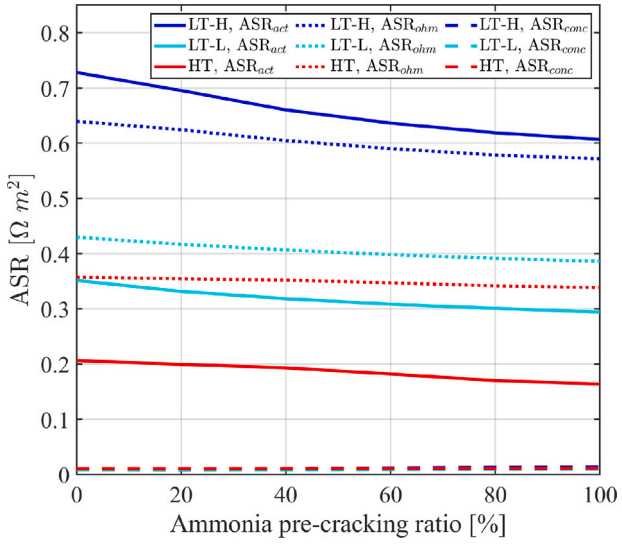

Fig. 10. Average area specific resistances (ASRs) for low temperature (LT) condition (600–700 °C) and (b) high temperature (HT) condition (700–800 °C) under various ammonia pre-cracking ratios. LT-L and LT-H refer to cases operating under low temperature conditions with the cells designed for low and high temperature operation, respectively.

prediction is presented in our previous study for an ammonia-fueled SOFC at cell level [41].

3.3.1. *Effect of location in the SOFC stack*

Fig. 11a shows the $K_n/K_{n,cr}$ ratio on six different lines at different locations (for locations see Fig. 11b) alongside the active area for the LT-00% crack case. The red-shaded region represents the area where $K_n/K_{n,cr} > 1$, indicating the potential for Ni nitriding to occur. The locations are specified in the legend in Fig. 11a. In the y-direction, $K_n/K_{n,cr}$ continuously decreases as ammonia cracks inside the stack. In the x-direction, by moving from the center to the sides, $K_n/K_{n,cr}$ increases. This is mainly attributed to the location of the fuel manifolds at the sides of the stack, which provides higher fuel flow rates along the sides of the stack. This results in lower residence time of ammonia on the catalyst layers there and consequently lower cracking rate of ammonia and higher values of $K_n/K_{n,cr}$ at the side of the active area (lines 4, 5, and 6) compared to middle (lines 1, 2, and 3).

In the z-direction, the lowest magnitude of $K_n/K_{n,cr}$ is observed at the center of the active area (z = 0 mm). The highest $K_n/K_{n,cr}$ values are present at the bottom of the stack. As the bottom is close to the fuel inlet and outlet (for inlet and outlet see Fig. 3d), the fuel flow rate is higher here (lines 3 and 6 in Fig. 3b), leading to a shorter residence time of ammonia on Ni layers and lower cracking rate of ammonia. High $K_n/K_{n,cr}$ values can also be found along the top lines (lines 2 and 5) as well, despite the lower flow rates here than at the center lines

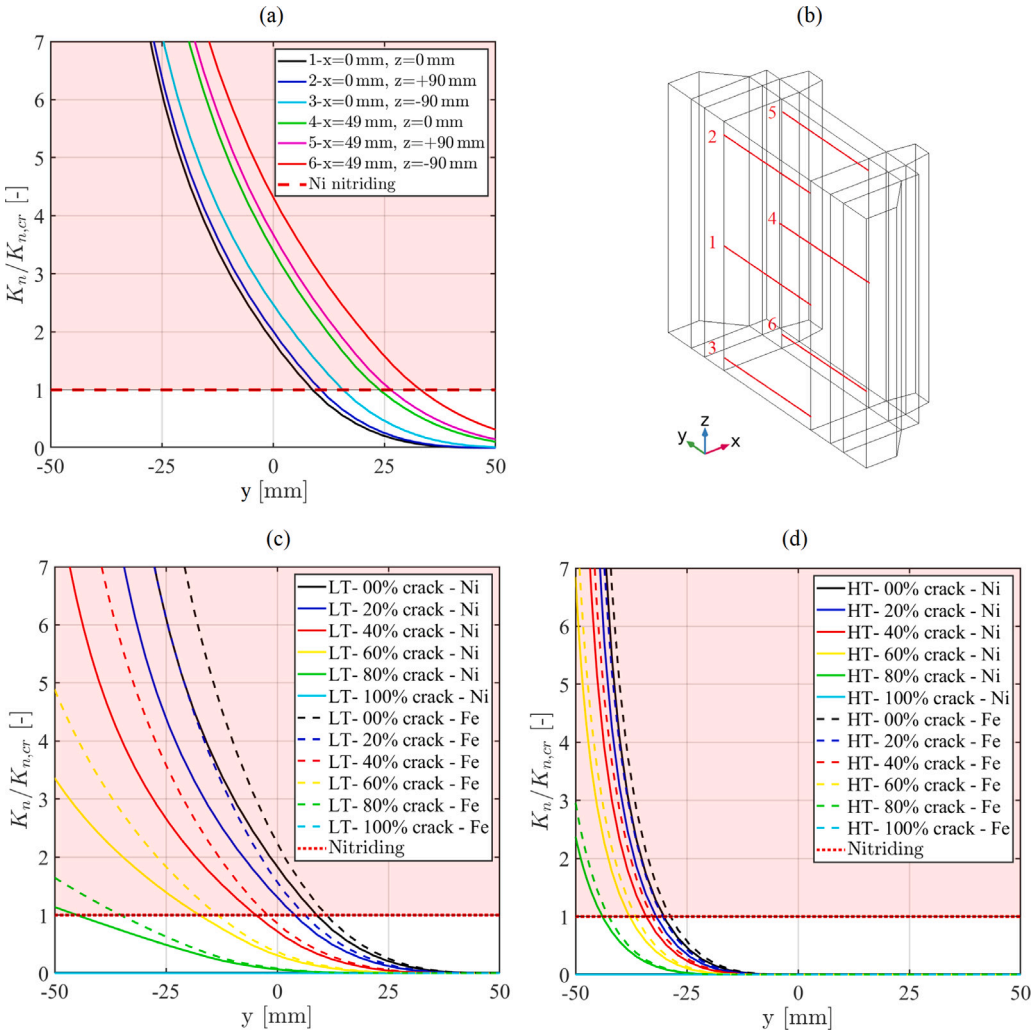

Fig. 11. (a) The $K_n/K_{n,cr}$ ratio on six different lines at different locations alongside the active area for the LT-00% crack case. Locations of lines are illustrated in (b). Distribution of the ratio of $K_n/K_{n,cr}$ inside the stack on the center line (line 1) alongside the active area for (c) low temperature (LT) condition (600–700 °C) and (d) high temperature (HT) condition (700–800 °C) under various ammonia pre-cracking ratios for Ni and Fe.

(lines 1 and 4). This is because, stack temperature is lower at the top and bottom than at the center, which leads to a slightly lower ammonia cracking rate and consequently higher $K_n/K_{n,cr}$ values. Therefore, it can be concluded that in the current design of the SOFC stack, the Ni nitriding potential is not uniform in the three dimensions, and 3D modeling is needed to capture the local potential of Ni nitriding. This is also the case for other quantities, although not shown explicitly here.

3.3.2. *Effect of fuel composition and operating temperature*

Fig. 11c and d depict the distribution of the $K_n/K_{n,cr}$ ratio inside the SOFC stack on the center line (line 1 in Fig. 11b) alongside the active area for LT and HT conditions under various ammonia pre-cracking ratios. The distribution of $K_n/K_{n,cr}$ for LT-L cases are similar to LT-H cases (not shown) due to the comparable distribution of ammonia and hydrogen (see Fig. 8a and b).

When none of the ammonia is pre-cracked (00% pre-crack cases), for the low temperature operation (LT case) more than half of the active area (~62 mm) is affected by the Ni nitriding (Fig. 11c), while the affected area for the HT case is only limited to around 22 mm over the active area (Fig. 11d). This is due to the lower cracking rate of ammonia at lower temperatures, which leads to more penetration of ammonia inside the SOFC stack (see Fig. 8) and consequently higher risk of Ni nitriding. Therefore, both low and high temperature cell technologies need pre-cracking to avoid nitriding, with a greater necessity for pre-cracking in the low-temperature cells.

As expected, by increasing the ammonia pre-cracking ratio, the Ni nitriding potential ($K_n/K_{n,cr}$) decreases due to lower ammonia content in the fuel stream. An interesting observation from Fig. 11c and d is that the $K_n/K_{n,cr}$ value is higher for the HT cases at the start of active area (y = −50 mm) than that in the LT cases. This difference is completely clear by comparison of 60% and 80% crack cases for the LT and HT cases. This is due to the reduction of $K_{n,cr}$ by increasing the temperature as shown in Fig. 2. As a result, under HT operating conditions, higher ratios of ammonia pre-cracking (~92% pre-cracking) are necessary compared to LT conditions (~82% pre-cracking) to effectively eliminate Ni nitriding.

The high amount of pre-cracking needed to run the systems safely points to that it might not be worth aiming for a system with a partial pre-cracking, as control of the flows is not straightforward compared to the marginal amount of ammonia that could be cracked in the stack in the pre-cracked cases. Perhaps it is better to pre-crack as much as possible while knowing that the stack is still tolerant to some (around 10–20%) amount of ammonia (not ppb level as proton exchange membrane fuel cells).

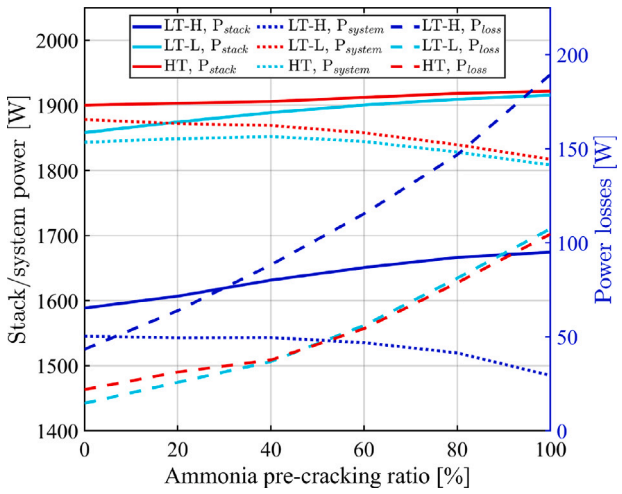

Fig. 12. Stack and system power and power losses (Eqs. (29) and (30)) for low temperature (LT) condition (600–700 °C) and high temperature (HT) condition (700–800 °C) under various ammonia pre-cracking ratios. LT-L and LT-H refer to cases operating under low temperature conditions with the cells designed for low and high temperature operation, respectively.

The Fe nitriding plots are also presented in Fig. 11c and d in the active area of the SOFC stack as a representative of steel's nitriding inside the SOFC stack. The $K_n/K_{n,cr}$ and nitriding potential is higher for Fe than Ni, which is mainly attributed to the lower $K_{n,cr}$ for Fe as depicted in Fig. 2b.

3.4. Effects of fuel composition and operating temperature on system level

The influence of the ammonia pre-cracking ratio and operating temperature of the SOFC stack on the system performance is investigated here. The concept of system modeling and the operating conditions are explained in Section 2.5. Fig. 12 shows the variation of stack and system power as well as power losses in the system for various ammonia pre-cracking ratios.

Stack power in the HT cases is around 15–20% higher than that in the LT-H cases due to lower ASRs and thus higher cell voltages. The stack power difference between the HT and LT-H cases is 19.6% and 14.8% for 00% crack and 100% crack cases, respectively. However, the stack power for HT and LT-L cases are rather similar to each other, especially at higher ammonia pre-cracking ratios. The produced power of the stack increases with increasing ammonia pre-cracking ratios due to the rise in the average temperature and reduction of ASRs (see Fig. 10) and consequently overpotentials.

The system power shows a similar trend with the stack power, which is higher for the HT cases compared to the LT-H cases. The system power is 21.5%, and 22.3% higher in the HT cases than their LT-H counterparts for 00% crack and 100% crack cases, respectively.

Despite the increase in the stack power with an increase in the ammonia pre-cracking ratio, the system power decreases as the ammonia pre-cracking ratio increases. This is mainly due to the higher required air flow rates in higher ammonia pre-cracking ratios (see Table 6) to maintain the stack temperature within the desired temperature range, with a maximum temperature variation of 100 °C. The higher air flow rate leads to higher pressure drops in the system and consequently higher power consumption in the system as shown in Fig. 12. The reduction in system power is more pronounced in the LT-H cases due to the higher rate at which the air flow rate increases with the increase in the ammonia pre-cracking ratio, compared to the HT cases.

It is worth mentioning that the anode off-gas recirculation (AOR) is not investigated in the current study, which has a significant impact on the system efficiency [41,53]. Therefore, only the power is reported to avoid misinterpretation regarding the ammonia-fueled SOFC system's potential efficiency. The efficiency of the system for HT cases is around 51–53% which can be improved significantly by implementing AOR. This will be investigated in future works by a comprehensive study of different system designs.

It should also be mentioned that the external cracker is considered to be designed to crack close to the desired amount of ammonia at both low and high temperature operating conditions. Nonetheless, it is important to highlight that efficient operation of ammonia cracking under low temperatures necessitates the presence of a better catalyst or a correspondingly larger cracker. The high temperature cells require expensive steels to build a stack while much cheaper catalysts such as iron (Fe), nickel (Ni), copper (Cu), and 304 stainless steel (304) [54] can be utilized in the external cracker due to the available high temperature heat in the system. On the other hand, cheaper steels can be used in the low temperatures stacks, while a much more novel and expensive catalyst such as ruthenium (Ru) based catalysts [55] may be needed for ammonia cracking under low temperature conditions. Therefore, there is trade-off between the cost of SOFC stack and external ammonia cracker for low and high temperature operating conditions.

4. Conclusion

In the current study, the effects of operating temperature and ammonia pre-cracking ratio on the reliability and performances of the ammonia-fueled solid oxide fuel cell (SOFC) stack and the overall system are investigated. In this context, a novel multiscale modeling approach has been developed, which combines a 3D multiphysics simulation of the ammonia-fueled SOFC stack with system-level modeling. Two kinds of cell technologies designed for low temperature (LT) and high temperature (HT) operation were compared. The cells were investigated under LT range from 600 to 700 °C, and a HT range from 700 to 800 °C. To have an idea of the influence of cell type on the performance under similar conditions, both of the cell technologies designed for LT and HT conditions are investigated under low temperature conditions, referred to as LT-L and LT-H cases, respectively. These investigations were conducted across a range of ammonia pre-cracking ratios including 0%, 20%, 40%, 60%, 80%, and 100%. The main findings can be summarized as follows:

* In the cases without ammonia pre-cracking, the inlet fuel temperature should be provided at 18 °C and 55 °C higher than the desired minimum operating temperature for LT and HT conditions, respectively. This is due to the cooling from the ammonia cracking, which is more intense and localized in the HT cases with faster cracking rates.
* The required air flow rate to maintain the SOFC stack temperature within the targeted range of 100 °C variation is increased by ammonia pre-cracking ratio, as cracking diminishes the cooling effect of the ammonia cracking. The increase in the required air flow rate for cooling of the stack in the 100% pre-cracking case compared to the 0% case is around 100% for the high temperature cells (HT and LT-H) while it is 216% for the low temperature cells (LT-L). Also, higher air flow rates are required for the LT-H cases than LT-L and HT cases.
* The current density distribution in the active area shows an opposite trend for the LT and HT cases. For the LT cases, current density increases from the start to the end of the active area, while it decreases in the HT cases. Furthermore, higher ammonia pre-cracking rates lead to more uniform and less uniform current density distribution under LT and HT conditions, respectively.
* Nitriding problems become significantly more pronounced under LT conditions, where more than half of the active area (~62 mm) experiences Ni nitriding, compared to HT cases where only around 22 mm is affected. On the other hand, achieving complete elimination of Ni nitriding demands a higher pre-cracking ratio at HT conditions (~92%) in comparison with LT conditions (~82%).

* The system power for HT and LT-L cases is comparable due to close SOFC stack power and power losses in the system. The system power of LT-H cases is significantly lower (approximately 22%) compared to their HT counterparts, primarily due to the decreased stack power and increased power losses in the system.
* The lower stack outlet temperatures in LT cases require novel and more expensive catalysts or correspondingly larger cracker for the cracking of the ammonia as compared to the catalyst and size of cracker to be used for cracking at higher operating temperatures. Operation temperature will therefore play in on the techno-economic balance between the lower cost of steel for the stack but higher catalyst cost for the pre-cracker at LT and vice-versa for HT.

This work highlights the importance and capability of the developed multiscale 3D/system modeling for ammonia-fueled SOFC simulation, taking into account the intricate multiphysics phenomena involved. The developed model can be utilized to further consider different aspects of the reliability and performance of ammonia-fueled SOFC stacks and systems. The direct coupling also makes it feasible to make dynamic simulations of the entire system and stack together.

CRediT authorship contribution statement

Arash Nemati: Writing – original draft, Visualization, Validation, Software, Methodology, Investigation, Conceptualization. **Omid Babaie Rizvandi:** Writing – review & editing, Validation, Software, Conceptualization. **Rafael Nogueira Nakashima:** Writing – review & editing, Methodology. **Javid Beyrami:** Writing – review & editing, Methodology. **Henrik Lund Frandsen:** Writing – review & editing, Supervision, Software, Investigation, Funding acquisition, Conceptualization.

Declaration of competing interest

The authors declare that they have no known competing financial interests or personal relationships that could have appeared to influence the work reported in this paper.

Data availability

The data that has been used is confidential.

Declaration of generative AI and AI-assisted technologies in the writing process

During the preparation of this work the authors used chat.openai.com in order to check the grammar. After using this tool/service, the authors reviewed and edited the content as needed and take full responsibility for the content of the publication.

Acknowledgments

The authors gratefully acknowledge the financial support from the project AMON. The project is supported by the Clean Hydrogen Partnership and its members Hydrogen Europe and Hydrogen Europe Research, under grant agreement No 101101521. Part of the computations were performed using the Sophia HPC cluster at the Technical University of Denmark (DTU).

Co-funded by the European Union. Views and opinions expressed are however those of the author(s) only and do not necessarily reflect those of the European Union or the Clean Hydrogen Partnership. Neither the European Union nor the granting authority can be held responsible for them.

Appendix A. Ammonia cracking rate validation on Ni-YSZ layers

Ammonia cracking rate plays an important role in the performance of the ammonia-fueled SOFCs as it affects the distributions of hydrogen, current density, and temperature over the active area. Therefore, the validity of the ammonia cracking rate developed by Kishimoto et al. [30] is examined against the experimental data reported in [30]. Here, a 2D model is developed for the test that was used for the validation of the developed ammonia cracking rate in [30]. Fig. A.1 shows the modeling domain consisting of the Ni-YSZ catalyst layer, YSZ substrate layer, two quartz layers, and fuel channel. Dimensions of different layers are listed in Table A.1. Similar to the 2D model presented in [30], transport equations of mass, momentum, species, and energy are coupled and solved numerically.

Table A.1
Dimensions of the different layers in the 2D model of ammonia cracking on Ni-YSZ catalyst [30].

Region	Dimension [mm]
Ni-YSZ catalyst length	10, 20, 40
Ni-YSZ catalyst thickness	0.017
YSZ substrate thickness	0.500
Fuel channel height at the middle of domain	1.483
Quartz layer thickness at top and bottom	2.000

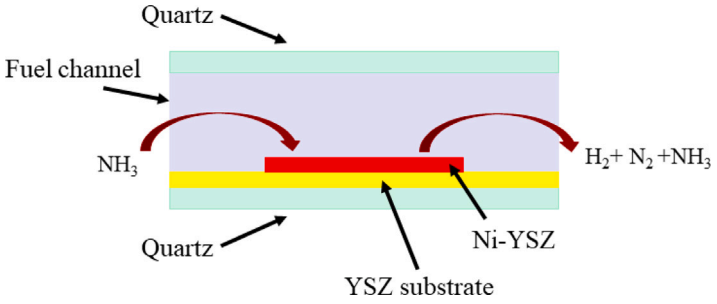

Fig. A.1. Schematic of the 2D model used for the ammonia cracking on the planar Ni-YSZ catalyst [30].

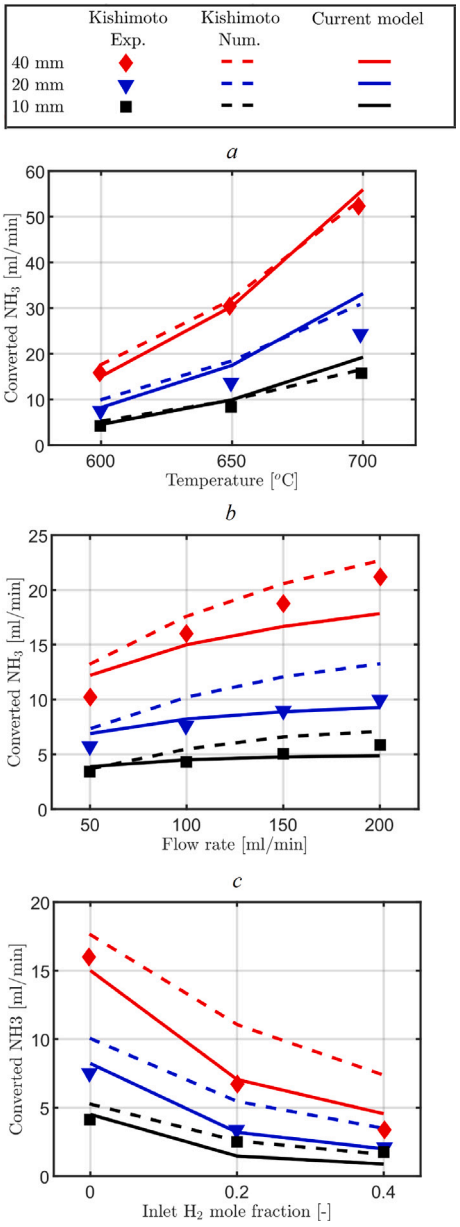

Fig. A.2. Comparison of the ammonia cracking rate between the current model, Kishimoto [30] experimental results (Exp.) and numerical results (Num.).

The fuel inlet boundary condition is considered to be fully developed and a volumetric flow rate is imposed on the fuel inlet boundary. All volume flow rates in the experimental study [30] are reported at the standard state. Therefore, the imposed volumetric flow rates at the inlet boundary are adjusted according to the operating temperatures. For the ammonia cracking rate, the developed correlation by Kishimoto et al. [30] is utilized which is presented in Eq. (1).

The results of the developed 2D model are compared with the experimental and numerical data reported in [30] in Fig. A.2. The experimental tests are reported at different operating temperatures, volumetric flow rates, and mole fractions of H_2 at the inlet [30] which are summarized in Table A.2. These comparisons are carried out at three different lengths of the Ni-YSZ catalyst layer, including 10 mm, 20 mm, and 40 mm. The results of the cracking rate obtained from the developed 2D model in the current study at different operating conditions are shown in Fig. A.2a, b, and c which show a reasonable agreement with the experimental data.

Table A.2
Operating conditions for ammonia cracking tests reported in Ref. [30].

Parameter	Fig. A.2-a	Fig. A.2-b	Fig. A.2-c
Temperature [°C]	600, 650, 700	600	600
Volumetric flow rate [ml/min]	100	50, 100, 150, 200	100
Inlet H2 mole fraction [–]	0.0	0.0	0.0, 0.2, 0.4

Appendix B. Validation of model and parameters for low temperature cell

A comparison of the experimental polarization curves and the values obtained from the simulation based on parameters reported in Table 2 is presented in Fig. B.1 for low temperature (Elcogen) cells. As can be seen, a good match is achieved between the experimental and simulation curves for all operating conditions under different current densities.

Appendix C. Validation of cell level model for ammonia-fueled SOFC for high temperature cell

In this section, the cell level model is validated for the pre-cracked ammonia (H_2+N_2) and direct ammonia (NH_3) fueled SOFCs for the high temperature cells. The 3D detailed model that is used for validation is comprehensively explained in the recent study [41]. The operating conditions of the experimental tests which are used for the validation of the model are explained in Table C.1.

Fig. C.1a and b shows the comparison of the experimental and numerical results under different operating conditions. As can be seen, there is a good agreement between the numerical simulation results and experimental data. This proves that the developed numerical model is able to capture the physics under both direct and pre-cracked ammonia-fueled conditions reasonably well.

The cell temperature is measured at the cathode side in the experimental tests that indicate around 8–10 °C temperature reduction compared to the test temperature (furnace temperature) due to endothermal cracking of NH_3. Fig. C.1c and d show the cell temperature at the air side for operating temperatures of 750 and 850 °C. As can be seen, the numerical results correspond well with the measurements i.e. a temperature drop of 8–10 °C. It is noteworthy that the temperature reduction is higher and more localized for the 850 °C case than that of 750 °C. This is because of the higher cracking rate of ammonia at higher temperatures. It is also noteworthy that in these tests, the cell test house is located inside a furnace. This leads to heat transfer between the cell test house and the surrounding ambient which is the furnace with a controlled temperature. Therefore, the cell temperature in the test is probably different from the cell temperature inside a stack that is isolated under the same operating conditions.

Appendix D. Validation of homogenized stack model for hydrogen fuel

The accuracy of the homogenized model has previously been analyzed in another study [48] by our research team as shown in Fig. D.1. In this study [48], the homogenized model is used to simulate the 18-cell FZJ Mark-F SOFC stack from Ref. [52] with hydrogen fuel. As shown in Fig. D.1b, the homogenized model is able to accurately predict the voltage and local temperature in a wide range of current densities. The operating conditions for the experiments conducted in Ref. [52] are represented in Table D.1.

It is worth mentioning that there are also further ongoing studies (not shown here) on using the homogenized model to simulate and investigate other commercial SOFC stacks operating with hydrogen and nitrogen mixtures representing the pre-cracked ammonia fuel. All of these studies show the validity and accuracy of the homogenized model in the prediction of underlying physical phenomena inside SOFC stacks.

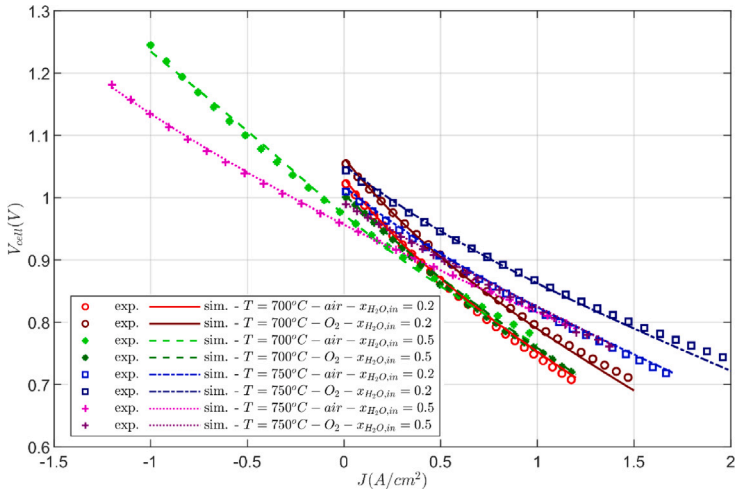

Fig. B.1. Comparisons of the polarization curves from the experimental data (exp) and simulation (sim) with the parameters reported in Table 2 for low temperature cells.

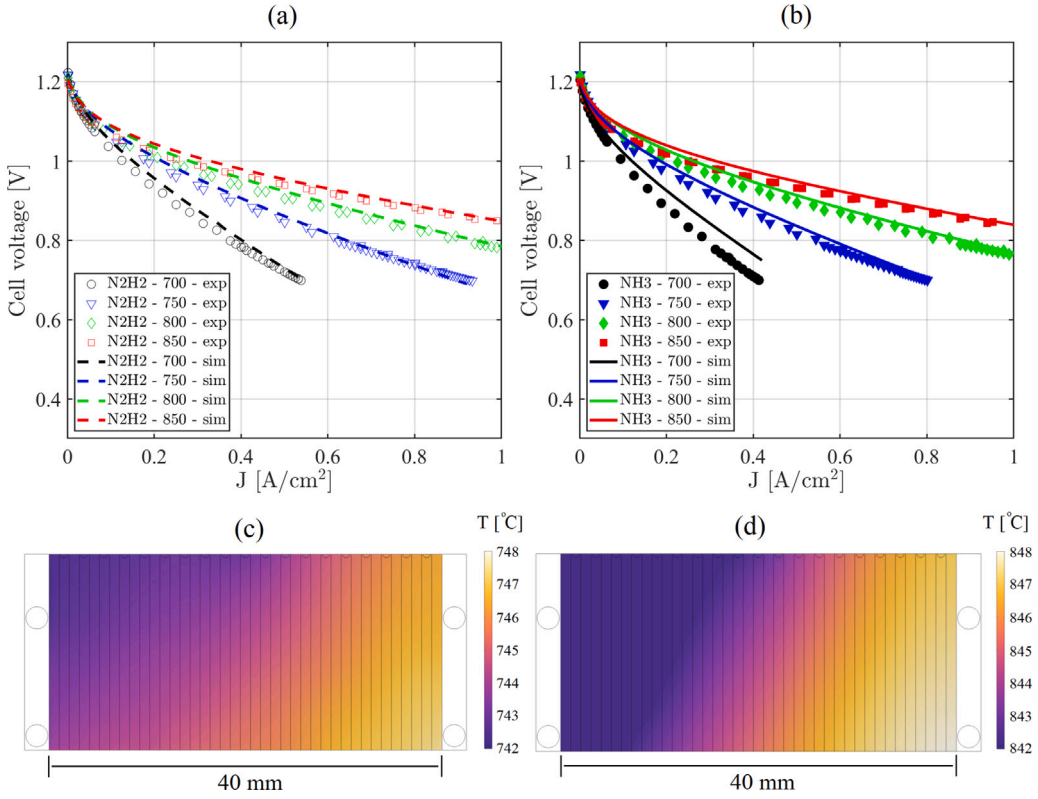

Fig. C.1. Comparisons of the polarization curves from simulation and experimental data under (a) pre-cracked ammonia, and (b) direct ammonia. Distribution of temperature on the air side of the cell for direct ammonia SOFC at (c) 750 and (d) 850 °C [41]. The fuel flow direction in (e) and (f) is left to right.

Table C.1
The operating conditions of the tests for direct and pre-cracked ammonia-fueled cases which are used for validation.

Direct/pre-cracked	Temperature [°C]	NH_3 [Nl/h]	H_2 [Nl/h]	N_2 [Nl/h]
Direct	700, 750, 800, 850	16	0	0
Pre-cracked	700, 750, 800, 850	0	24	8

Table D.1
Operating conditions for the SOFC stack tests reported in Ref. [52].

Parameter	Dimension [mm]
Load current density	0–0.8 [A/cm^2]
Flows inlet temperature	675 [°C]
Furnace temperature	750 [°C]
Hydrogen inlet flow rate	90 [slpm]
Steam inlet flow rate	10 [slpm]
Air inlet flow rate	307 [slpm]

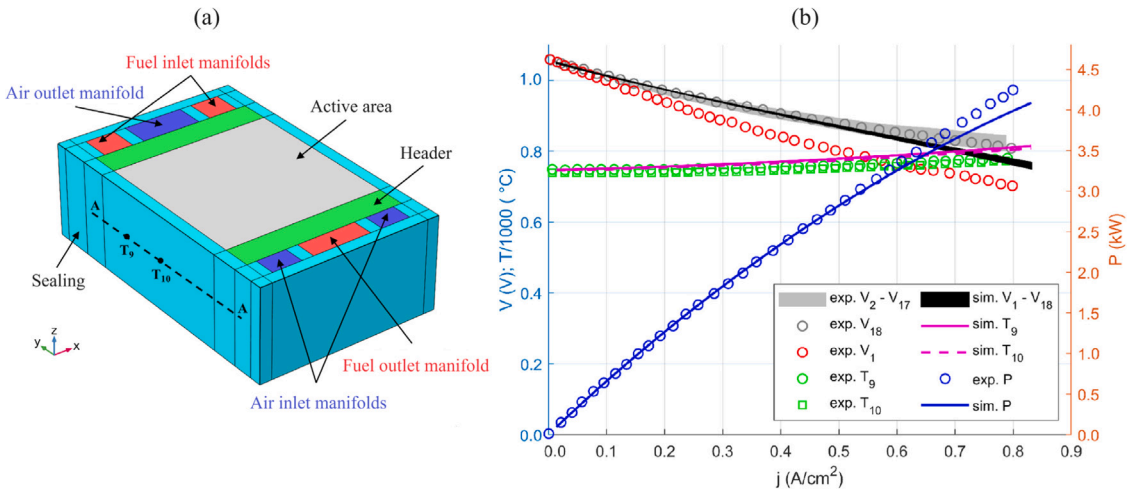

Fig. D.1. Homogenized stack model validation against the experimental data from Nishida et al. [52] for the 18-cell FZJ Mark-F SOFC stack: (a) Schematic of the SOFC stack configuration. Locations of the temperature probes T_9 and T_{10} are shown in this figure; and (b) comparisons of the polarization, temperature, and power curves for different current densities. The abbreviations exp and sim denote experiment and simulation data, respectively. Voltage subscripts represent the cell number, 1 for the bottom cell and 18 for the top cell [48].

References

[1] Christopher S, Vikram M, Bakli C, Thakur AK, Ma Y, Ma Z, Xu H, Cuce PM, Cuce E, Singh P. Renewable energy potential towards attainment of net-zero energy buildings status–a critical review. J Clean Prod 2023;136942.

[2] Hossain MB, Islam MR, Muttaqi KM, Sutanto D, Agalgaonkar AP. Advancement of fuel cells and electrolyzers technologies and their applications to renewable-rich power grids. J Energy Storage 2023;62:106842.

[3] Feng Y, Qu J, Zhu Y, Wu B, Wu Y, Xiao Z, Liu J. Progress and prospect of the novel integrated SOFC-ICE hybrid power system: System design, mass and heat integration, system optimization and techno-economic analysis. Energy Convers Manage: X 2023;100350.

[4] Wang L, Zhang Y, Pérez-Fortes M, Aubin P, Lin T-E, Yang Y, Maréchal F, et al. Reversible solid-oxide cell stack based power-to-x-to-power systems: Comparison of thermodynamic performance. Appl Energy 2020;275:115330.

[5] Wan Z, Tao Y, Shao J, Zhang Y, You H. Ammonia as an effective hydrogen carrier and a clean fuel for solid oxide fuel cells. Energy Convers Manage 2021;228:113729.

[6] Andriani D, Bicer Y. A review of hydrogen production from onboard ammonia decomposition: Maritime applications of concentrated solar energy and boil-off gas recovery. Fuel 2023;352:128900.

[7] Comotti M, Frigo S. Hydrogen generation system for ammonia–hydrogen fuelled internal combustion engines. Int J Hydrog Energy 2015;40(33):10673–86.

[8] Machaj K, Kupecki J, Malecha Z, Morawski A, Skrzypkiewicz M, Stanclik M, Chorowski M. Ammonia as a potential marine fuel: A review. Energy Strategy Rev 2022;44:100926.

[9] Hagen A, Langnickel H, Sun X. Operation of solid oxide fuel cells with alternative hydrogen carriers. Int J Hydrog Energy 2019;44(33):18382–92.

[10] Sonker M, Tiwary SK, Shreyash N, Bajpai S, Ray M, Kar SK, Balathanigaimani M. Ammonia as an alternative fuel for vehicular applications: Paving the way for adsorbed ammonia and direct ammonia fuel cells. J Clean Prod 2022;133960.

[11] Rizvandi OB, Nemati A, Nami H, Hendriksen PV, Frandsen HL. Numerical performance analysis of solid oxide fuel cell stacks with internal ammonia cracking. Int J Hydrog Energy 2023.

[12] Yang J, Molouk AFS, Okanishi T, Muroyama H, Matsui T, Eguchi K. A stability study of Ni/yttria-stabilized zirconia anode for direct ammonia solid oxide fuel cells. ACS Appl Mater Interfaces 2015;7(51):28701–7.

[13] Ni D-W, Charlas B, Kwok K, Molla TT, Hendriksen PV, Frandsen HL. Influence of temperature and atmosphere on the strength and elastic modulus of solid oxide fuel cell anode supports. J Power Sources 2016;311:1–12.

[14] Kishimoto M, Muroyama H, Suzuki S, Saito M, Koide T, Takahashi Y, Horiuchi T, Yamasaki H, Matsumoto S, Kubo H, et al. Development of 1 kW-class ammonia-fueled solid oxide fuel cell stack. Fuel Cells 2020;20(1):80–8.

[15] Stoeckl B, Subotić V, Preininger M, Schwaiger M, Evic N, Schroettner H, Hochenauer C. Characterization and performance evaluation of ammonia as fuel for solid oxide fuel cells with Ni/YSZ anodes. Electrochim Acta 2019;298:874–83.

[16] Stoeckl B, Preininger M, Subotić V, Megel S, Folgner C, Hochenauer C. Towards a wastewater energy recovery system: The utilization of humidified ammonia by a solid oxide fuel cell stack. J Power Sources 2020;450:227608.

[17] Pfeifer T, Chakradeo A, Ahire N, Baade J, Barthel M, Dosch C, Näke R, Hartmann M. Development of a SOFC power generator for the Indian market. Fuel Cells 2017;17(4):550–61.

[18] Su H, Hu YH. Progress in low-temperature solid oxide fuel cells with hydrocarbon fuels. Chem Eng J 2020;402:126235.

[19] Zhang Y, Knibbe R, Sunarso J, Zhong Y, Zhou W, Shao Z, Zhu Z. Recent progress on advanced materials for solid-oxide fuel cells operating below 500 c. Adv Mater 2017;29(48):1700132.

[20] Boldrin P, Brandon NP. Progress and outlook for solid oxide fuel cells for transportation applications. Nat Catal 2019;2(7):571–7.

[21] Wachsman ED, Lee KT. Lowering the temperature of solid oxide fuel cells. Science 2011;334(6058):935–9.

[22] Kishimoto M, Kume T, Iwai H, Yoshida H. Numerical analysis of ammonia-fueled planar solid oxide fuel cells. ECS Trans 2017;78(1):2845.

[23] Oh S, Oh MJ, Hong J, Yoon KJ, Ji H-I, Lee J-H, Kang H, Son J-W, Yang S. A comprehensive investigation of direct ammonia-fueled thin-film solid-oxide fuel cells: Performance, limitation, and prospects. Iscience 2022;25(9):105009.

[24] Rokni M. Addressing fuel recycling in solid oxide fuel cell systems fed by alternative fuels. Energy 2017;137:1013–25.

[25] Peters R, Deja R, Engelbracht M, Frank M, Blum L, Stolten D, et al. Efficiency analysis of a hydrogen-fueled solid oxide fuel cell system with anode off-gas recirculation. J Power Sources 2016;328:105–13.

[26] Selvam K, Komatsu Y, Sciazko A, Kaneko S, Shikazono N. Thermodynamic analysis of 100% system fuel utilization solid oxide fuel cell (SOFC) system fueled with ammonia. Energy Convers Manage 2021;249:114839.

[27] Quach T-Q, Giap V-T, Lee DK, Israel TP, Ahn KY. High-efficiency ammonia-fed solid oxide fuel cell systems for distributed power generation. Appl Energy 2022;324:119718.

[28] Meng T, Cui D, Shi Y, Ji Y, Cheng M, Tu B, Lan Z. Performance evaluation of high-efficiency SOFC-PEMFC hybrid system fueled by liquid ammonia. Int J Hydrog Energy 2023;48(79):30887–98.

[29] Qu J, Feng Y, Zhu Y, Wu B, Liu J, Jing H, Gao Y. Thermodynamic analysis and comprehensive system optimization of the near zero emission hybrid power based on SOFC-ICE integrated system fueled with ammonia. Energy Convers Manage 2023;294:117553.

[30] Kishimoto M, Furukawa N, Kume T, Iwai H, Yoshida H. Formulation of ammonia decomposition rate in Ni-YSZ anode of solid oxide fuel cells. Int J Hydrog Energy 2017;42(4):2370–80.

[31] Trini M, De Angelis S, Jø rgensen P, Hauch A, Chen M, Hendriksen P. Phase field modelling of microstructural changes in Ni/YSZ solid oxide electrolysis cell electrodes. In: In proceedings of the 42nd international conference on advanced ceramics and composites, ceramic engineering and science proceedings. vol. 2, 2018, p. 165.

[32] Ni M. Thermo-electrochemical modeling of ammonia-fueled solid oxide fuel cells considering ammonia thermal decomposition in the anode. Int J Hydrog Energy 2011;36(4):3153–66.

[33] Lehrer E. Über das Eisen-Wasserstoff-Ammoniak-Gleichgewicht. Z Elektrochemie Angew Phys Chem 1930;36(6):383–92.

[34] Yang M, Sisson Jr R. Modeling the nitriding process of steels. Adv Mater Process 2012;170(7):33–7.

[35] Yang M, Sisson R. Gaseous nitriding process control: application of customised lehrer diagrams. Int Heat Treat Surf Eng 2013;7(4):164–71.

[36] Fonović M, Leineweber A, Mittemeijer EJ. Experimental investigation and thermodynamic modeling of the Ni-rich part of the Ni-n phase diagram. Metall Mater Trans A 2014;45:4863–74.

[37] Rizvandi OB, Nemati A, Chen M, Frandsen HL. A numerical investigation of nitridation in solid oxide fuel cell stacks operated with ammonia. Int J Hydrog Energy 2023;50:961–76.
[38] Wriedt H. The N-Ni (nitrogen-nickel) system. Bull Alloy Phase Diagr 1985;6(6):558–63.
[39] Kim S, Yoon S, Kim J-H, Park S. The effect of the transformation of ε-Fe2-3n into γ-Fe4N phase on the fatigue strength of gas-nitrided pure iron. Metals 2020;10(6):823.
[40] Saffirio S, Pylypko S, Fiorot S, Schiavi I, Fiore S, Santarelli M, Ferrero D, Smeacetto F, Fiorilli S. Hydrothermally-assisted recovery of yttria-stabilized zirconia (YSZ) from end-of-life solid oxide cells. Sustain Mater Technol 2022;33:e00473.
[41] Nemati A, Rizvandi OB, Mondi F, Frandsen HL. Detailed 3D multiphysics modeling of an ammonia-fueled solid oxide fuel cell: Anode off-gas recirculation and Ni nitriding degradation. Energy Convers Manage 2024;308:118396.
[42] Bilalis V, Sun X, Frandsen HL, Chen M. Quantifying galvanostatic degradation of solid oxide electrolysis cells: The onset of accelerated degradation of Ni-yttria stabilized zirconia electrode. J Power Sources 2024;606:234490.
[43] Navasa M, Miao X-Y, Frandsen HL. A fully-homogenized multiphysics model for a reversible solid oxide cell stack. Int J Hydrog Energy 2019;44(41):23330–47.
[44] Leonide A, Apel Y, Ivers-Tiffee E. SOFC modeling and parameter identification by means of impedance spectroscopy. ECS Trans 2009;19(20):81.
[45] Ni M, Leung MK, Leung DY. Parametric study of solid oxide steam electrolyzer for hydrogen production. Int J Hydrog Energy 2007;32(13):2305–13.
[46] Liu S, Kong W, Lin Z. Three-dimensional modeling of planar solid oxide fuel cells and the rib design optimization. J Power Sources 2009;194(2):854–63.
[47] Beyrami J, Nakashima RN, Nemati A, Frandsen HL. Degradation modeling in solid oxide electrolysis systems: a comparative analysis of operation modes. Energy Convers Manage:X 2024;100653.
[48] Rizvandi OB, Miao X-Y, Frandsen HL. Multiscale modeling of degradation of full solid oxide fuel cell stacks. Int J Hydrog Energy 2021;46(54):27709–30.
[49] Rizvandi OB, Frandsen HL. Modeling of single-and double-sided high-pressure operation of solid oxide electrolysis stacks. Int J Hydrog Energy 2023;48(77):30102–19.
[50] Yu S, Zhang S, Schäfer D, Peters R, Kunz F, Eichel R-A. Numerical modeling and simulation of the solid oxide cell stacks and metal interconnect oxidation with openfoam. Energies 2023;16(9):3827.
[51] Miao X-Y, Rizvandi OB, Navasa M, Frandsen HL. Modelling of local mechanical failures in solid oxide cell stacks. Appl Energy 2021;293:116901.
[52] Nishida R, Beale S, Pharoah J, de Haart L, Blum L. Three-dimensional computational fluid dynamics modelling and experimental validation of the Jülich mark-f solid oxide fuel cell stack. J Power Sources 2018;373:203–10.
[53] Rizvandi OB, Nemati A, Frandsen HL. A numerical study of fuel recirculation in ammonia-fueled solid oxide fuel cell stacks. Int J Hydrog Energy 2024;53:792–806.
[54] Zheng K, Yan Y, Sun Y, Yang J, Zhu M, Ni M, Li L. An experimental study of ammonia decomposition rates over cheap metal catalysts for solid oxide fuel cell anode. Int J Hydrog Energy 2023;48(50):19188–95.
[55] Asif M, Bibi SS, Ahmed S, Irshad M, Hussain MS, Zeb H, Khan MK, Kim J. Recent advances in green hydrogen production, storage and commercial-scale use via catalytic ammonia cracking. Chem Eng J 2023;145381.